Edge effect: Liquid sheet and droplets formed by drop impact close to an edge

S. Lejeune*
Microfluidics Lab, Department of Aerospace and Mechanical Engineering, University of Liège, 4000 Liège, Belgium and Fluid Dynamics of Disease Transmission Laboratory, Massachusetts Institute of Technology, Cambridge, Massachusetts 02139, USA

T. Gilet†
Microfluidics Lab, Department of Aerospace and Mechanical Engineering, University of Liège, 4000 Liège, Belgium

L. Bourouiba‡
Fluid Dynamics of Disease Transmission Laboratory, Massachusetts Institute of Technology, Cambridge, Massachusetts 02139, USA

(Received 29 January 2018; published 7 August 2018)

Asymmetric liquid sheet fragmentation is ubiquitous in nature and potentially shapes critical phenomena such as rain-induced propagation of foliar diseases. In this experimental study, we investigate the formation and fragmentation of a liquid sheet upon impact of a drop close to the edge of a solid substrate. Both the impact Weber number and the offset, the distance from the impact point to the edge, are systematically varied. Their influence on the kinematics of the liquid sheet and the subsequent statistics of droplet ejection are rationalized. Three major asymmetry scenarios are identified and linked to distinct droplet ejection patterns. Scaling laws are proposed to rationalize these scenarios based on impact parameters.

DOI: 10.1103/PhysRevFluids.3.083601

I. INTRODUCTION

Around 10% of the world's crops are still lost due to plant diseases [1], which costs billions of dollars each year [2,3] and increases pressure on communities [1]. The optimization of the timing and amount of sprayed chemicals in the context of smart agriculture requires improved understanding of disease spread in the field [4–7]. Rain was found to be correlated with the dispersal of foliar diseases such as Septoria leaf blotch and Fusarium head blight, affecting wheat and rice, respectively [8–10]. Prior studies mainly focused on dispersal statistics collected at the level of crop fields or parcels [9,11–13]. Investigations at the level of leaf and plant remain scarce [11,14–16]. They are statistical in nature, accounting for neither drop-plant interactions nor the underlying fragmentation physics. Thus, generalizing results to various plants and precipitations remains a challenge [7,17]. Recent studies have provided insight into raindrop-leaf interactions [18,19], identifying the important role of wetting and of sessile drops on leaves. They identified several dispersal mechanisms as a function of leaf mechanical properties that are both common and efficient at dispersing pathogens. One of the

*slejeune@uliege.be
†tristan.gilet@uliege.be
‡lbouro@mit.edu

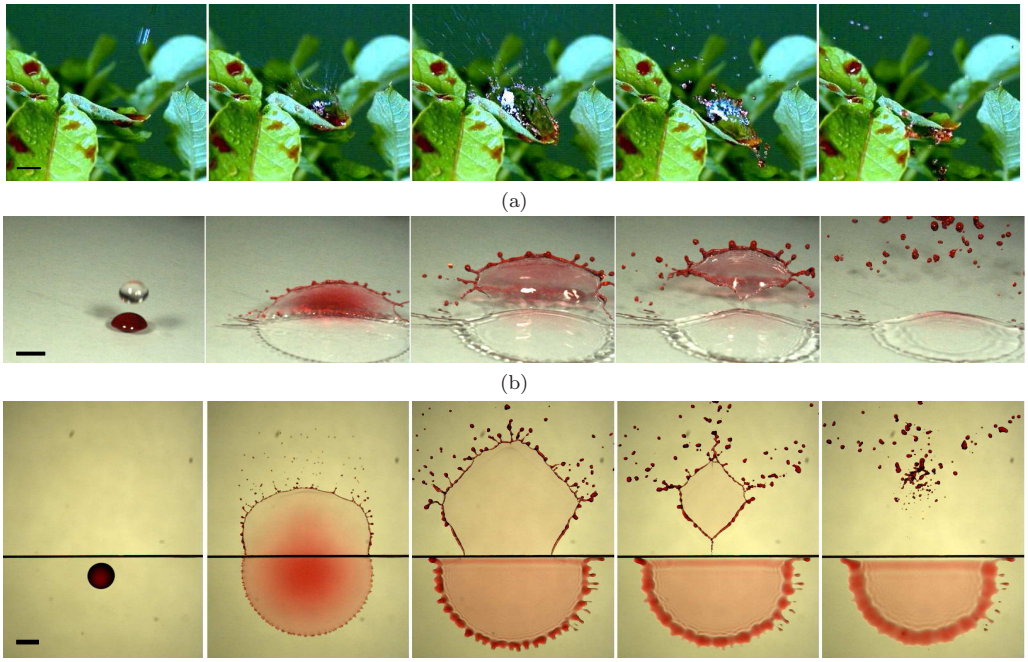

FIG. 1. Liquid sheet formation and fragmentation into droplets, in three configurations. (a) In the field, a raindrop impacts onto a potato leaf on which dyed fluid (red) was deposited. Times are, from left to right, −3, 2, 6, 13, and 29 ms with respect to impact. The sheet is fully three dimensional. (b) A water drop impacts close to a dyed sessile drop on a flat horizontal dry plexiglass substrate. Times are, from left to right, −1, 3, 8, 11, and 23 ms with respect to impact. The sheet is still fully three dimensional. (c) Impact of a dyed drop close to the edge of a flat dry plexiglass substrate. Times are, from left to right, 0, 2.5, 8, 10.5, and 14 ms from impact. The sheet remains largely in the plane of the substrate. Scale bars are 5 mm.

main dispersal scenarios on semirigid leaves, coined the crescent-moon scenario [Fig. 1(a)], consists in the impact of a raindrop in the vicinity of a sessile (contaminated) drop supported by the infected leaf. The sessile drop is stretched into an asymmetric liquid sheet, which then retracts and fragments into a myriad of contaminated droplets ejected away from the plant.

Drop impacts have been studied in many configurations [20–22] including impacts on thin films [23–25], on deep liquid layers [26,27], or on solid substrates with various wettings, geometries, and inclinations [21,28–32]. Impacts at sufficiently high speed result in a splash, which involves the formation of a liquid sheet, a crown, which then destabilizes into droplets. Previous studies focused on the crown dynamics and droplet ejection in axisymmetric configurations [33–37]. Increasing attention has also been paid to impacts on small solid targets of size comparable to that of the drop diameter [38–42] or binary drop collision [43,44]. In the crescent-moon impact scenario, an intrinsic horizontal asymmetry leads to a nonaxisymmetric liquid sheet [19]. The latter induces asymmetry in the speed and direction of ejected droplets. Inclination, compliance, and finite size of the leaves all amplify this asymmetry [19]. Drop impacts that yield asymmetric behaviors were also studied with (i) horizontal gradients of texture and wetting properties [45–50], (ii) varying inclination or tangential speed of the substrate [51–53], and (iii) nonaxisymmetric target shapes [54,55]. The relationship between liquid sheet asymmetry and droplet ejections was investigated for a stationary liquid sheet [56]. The mass distribution of ejected droplets has been quantified in [39]. By contrast, the distributions of droplet speed and direction were seldom reported and never fully investigated, though these variables are crucial to assess the dispersal of plant diseases via raindrop impact.

Our observation of a large number of drop impacts on wet leaves, in fields and in the laboratory [Figs. 1(a) and 1(b)], confirmed the frequent occurrence of asymmetric liquid sheets in the air. These sheets develop either through the crescent-moon scenario described in [18] or by impacts close to edge of leaves, or by a combination of both. The crescent-moon mechanism was reproduced in laboratory conditions with a drop impacting close to a sessile drop on a flat, dry, and rigid substrate [Fig. 1(b)]. The key emerging features are (i) the asymmetric shape of the sheet in the air, (ii) the fluid of this sheet originating mainly from the sessile drop, (iii) a destabilizing free rim at the outer edge of the sheet, and (iv) the presence of a triple solid-liquid-air contact line. The crescent-moon sheet is inherently three dimensional, hence complex to track accurately.

In this paper, we identify and study one of the simplest impact configurations that produces a sheet with the aforementioned features. It consists in the impact of a single drop close to the straight edge of a flat dry substrate [Fig. 1(c)]. Upon impact, the drop spreads radially until it reaches the edge. It then continues to expand in the air, thereby forming a liquid sheet whose asymmetry varies with the distance from the impact point to the edge. The main goal of this paper is to characterize the dynamics of this sheet and the number, mass, direction, and speed of the ejected droplets, as a function of impact speed and distance of impact point to the edge, referred to as offset. In Sec. II we present the experimental setup. We then describe the phenomenology of the liquid sheet expansion, retraction, and breakup for various impact speeds and offsets in Sec. III. A quantitative analysis of the sheet dynamics and the droplet statistics is presented in Secs. IV and V, respectively. Results and implications of the asymmetry of the liquid sheet in shaping droplet patterns in the context of rain-induced foliar pathogen dispersal are discussed in Sec. VI.

II. EXPERIMENTAL SETUP

A syringe pump is filled with dyed water, of surface tension $\sigma \simeq 70$ mN/m, density $\rho \simeq 1000$ kg/m^3, and kinematic viscosity $\nu \simeq 10^{-6}$ m^2/s at room temperature ($20\,^\circ\text{C} \pm 2\,^\circ\text{C}$). The syringe is connected to a vertical needle that releases drops of radius $R_0 = 2.4 \pm 0.03$ mm. These drops fall and impact near the edge of a flat horizontal substrate. This substrate is made of dry plexiglass, 2 mm thick, with advancing and receding contact angles for water of 85° and 55° ($70^\circ \pm 15^\circ$), respectively, cut straight with average roughness of 4 μm. The offset d is defined as the distance between the impact point and the straight edge, counted positively when at least half the drop hits the substrate. It is varied in the range $d/R_0 \in [-1, 5]$ with a millimeter stage. The parameters are summarized in Table I. The phenomenon is recorded from the top with a high-speed camera and using backlighting at 2000 frames per second. The inclination of the camera is less than 20° from the vertical and is accounted for in the image processing. The position and shape of the liquid sheet and the droplets are measured by image processing. Time interpolations of the motion allow for the detection of major events such as the impact of the drop and the entry of the sheet in the air. Five different impact speeds V_0 in the range 1.6–6 m/s were used by changing the height of the needle (Table I). The impact speed was determined as a function of the height of release in a different experiment, where the falling drops were filmed from the side. Slight oscillations and flattening of the incoming drop, observed during the free fall right before impact, did not appear to affect the impact dynamics at first order. Local defects that could be present on the edge favored the appearance of nucleation holes that developed from the edge. This generated a notable modification of the sheet dynamics and of its subsequent breakup pattern. This phenomenon is unmistakably identifiable, and we excluded on purpose the very few experiments in which it occurred. Figure 1(c) shows the process from impact to sheet collapse over 12.5 ms. The impact time of the drops scales as $t_i = 2R_0/V_0 \simeq 1$ ms (Table I). The sheet lifetime is closer to the capillary time $t_c = \sqrt{4\rho R_0^3/(3\sigma)} = 16.2$ ms. The Weber number $\text{We} = 2\rho R_0 V_0^2/\sigma \sim (t_c/t_i)^2$, the ratio of kinetic energy of the impacting drop to its surface energy, is much larger than unity for all our experiments (Table I). The Froude number squared $\text{Fr}^2 = V_0^2/(2gR_0)$ ranges between 50 and 800, allowing one to neglect hydrostatic pressure. Viscous effects can be neglected during impact given that the Ohnesorge number $\text{Oh} = \sqrt{\nu^2\rho/(2R_0\sigma)}$ is

TABLE I. List of variables and symbols with their definition and typical values.

Symbol	Meaning	Value or range (room temperature $\simeq 20\,^{\circ}$C)
	Physical properties and initial conditions	
d	offset	2.4–12 mm
R_0	initial drop radius	2.4 ± 0.03 mm
V_0	initial drop speed	$1.6, 2.3, 3.2, 4.4, 6 \pm 0.1$ m/s
M_0	initial drop mass ($M_0 = 4\pi R_0^3/3$)	57.9 ± 2 mg
ρ	water density	1000 kg/m^3
ν	water kinematic viscosity	10^{-6} m^2/s
σ	water surface tension	70 ± 2 mN/m
	Characteristic times and dimensionless numbers	
t_i	impact time $t_i = 2R_0/V_0$	2.9, 2.1, 1.5, 1.1, 0.8 ms
t_c	capillary time $t_c = \sqrt{4\rho R_0^3/(3\sigma)}$	16.2 ms
We	Weber number $\mathrm{We} = 2\rho R_0 V_0^2/\sigma$	186 (◯), 367 (▷), 700 (★), 1340 (□), 2435 (◇)
Oh	Ohnesorge number $\mathrm{Oh} = \sqrt{\nu^2\rho/(2R_0\sigma)}$	0.0017
Fr	Froude number $\mathrm{Fr}^2 = V_0^2/(2gR_0)$	50–800
	Sheet spreading on solid	
R_s	spreading radius on solid	(mm)
R_{sM}	maximum of R_s	(mm)
t_{sM}	time of R_{sM}	(s)
δ	dimensionless offset $\delta = d/R_{sM}$	
t_d	time at which the liquid reaches the edge of the substrate	(s)
	Sheet expansion in the air	
l_n	extension of the air sheet normal to the edge	(mm)
l_{nM}	maximum of l_n	(mm)
t_{nM}	time of l_{nM}	(s)
τ_n	dimensionless normal time $\tau_n = (t - t_d)/(t_{nM} - t_d)$	
l_t	extension of the air sheet tangential to the edge	(mm)
l_{tM}	maximum of l_t	(mm)
t_{tM}	time of l_{tM}	(s)
t_r	time of the sheet collapse along the edge	(s)
τ_r	dimensionless time of collapse along the edge $\tau_r = (t_r - t_d)/(t_{nM} - t_d)$	
	Droplet ejections	
v	horizontal ejection speed of a droplet	(mm/s)
v_T	average speed of droplets ejected at a given τ_n	(mm/s)
m	mass of a droplet	(mg)
$\Phi(X)$	maximal value of a variable X taken as the cutoff of its CDF	
x	distance traveled horizontally from ejection by a droplet	(mm)
Ψ	asymptotic value traveled by a droplet $\Psi = \lim_{t\to\infty} x$	(mm)
Ψ_M	maximum value of Ψ	(mm)
$Q_i(X)$	quantile function of a variable X taken at $i\%$	

0.0017 for the considered size of the impacting drop. In rainfalls, the diameter and terminal speed of raindrops range from 0.5 mm at 2 m/s to 5 mm at 9 m/s, respectively [57,58]. These parameters yield $\mathrm{We} \in [28, 5800]$, $\mathrm{Fr}^2 \in [800, 1700]$, and $\mathrm{Oh} \in [0.0017, 0.0053]$, fairly close to those considered in our experiments.

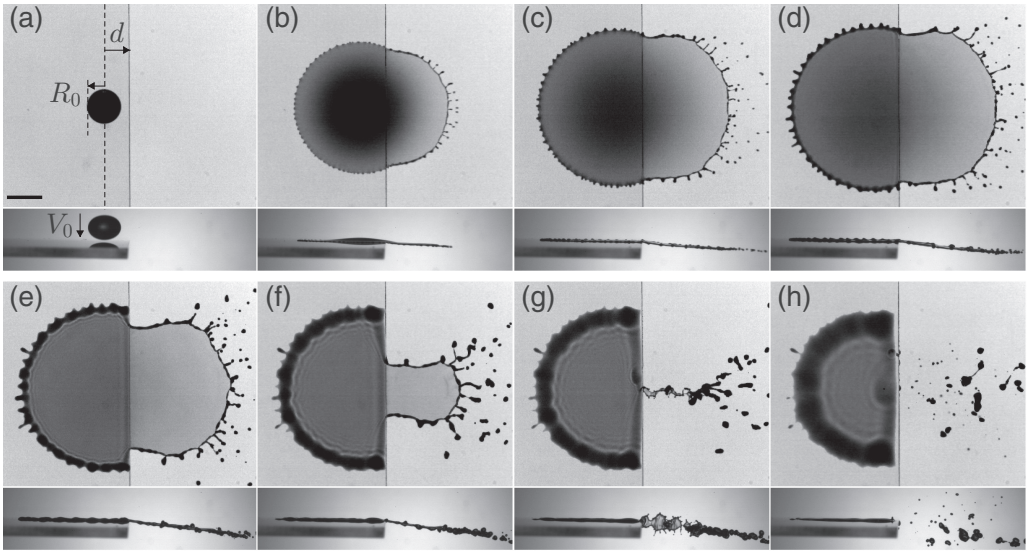

FIG. 2. Drop impact on a flat surface close to its edge, from top and side views. The radius of the impacting drop is $R_0 \simeq 2.4$ mm and the Weber number We $= 1340$. The offset d is defined as the distance between the impact point and the edge. The scale bar is 5 mm and the times are (a) $t = 0$, (b) $t = 1.6$, (c) $t = 3$, (d) $t = 4.4$, (e) $t = 7$, (f) $t = 10.6$, (g) $t = 12.4$, and (h) $t = 19$ ms after impact.

III. PHENOMENOLOGY

In Fig. 2, the impact near an edge is presented from synchronized top and side views. Along the edge, the extension of the liquid sheet in the air follows the spread on the solid [Figs. 2(b)–2(d)]. By contrast, the strong retraction of the sheet along the edge is desynchronized from the slight dewetting on top of the substrate [Figs. 2(e)–2(g)]. In the direction normal to the edge, the sheet extends further in the air than it spreads on the solid [Figs. 2(b)–2(d)]. The maximum extension of the sheet is reached first along the edge then normal to the edge [Fig. 2(e)]. The differences in these extension and retraction kinematics normal and tangent to the edge are key in shaping the asymmetric liquid sheet in the air. Droplets are emitted from the corrugated rim at the front of the sheet, as well as from the breakup of the filaments after the collapse of the sheet.

The side view in Fig. 2 shows that the sheet stays approximately in the plane of the substrate throughout the whole process. The droplets are also ejected in this plane, except during the final collapse of the sheet where the antagonistic movements of the rim along the edge give rise to out-of-plane ejections [Figs. 2(g)–2(h) side view]. The planar and almost horizontal movements of the sheet are crucial for the accuracy of geometric and kinematic measurements from the top view alone. We measured the inclination φ of the sheet from the vertical at its maximal expansion, as a function of offset d (Fig. 3). This inclination first increases linearly with d/R_0 and then reaches a plateau of mean value 87°, independent of We. This value below 90° could be explained by the slight hydrophilicity of the substrate [59,60] or by an imperfect transfer of momentum from vertical to horizontal during initial crushing and was also noted for symmetric impacts on poles [42]. A linear fit of the range $d/R_0 \in [0, 1]$ gives

$$\varphi \simeq 53\frac{d}{R_0} + 18. \tag{1}$$

The intersection of this fit with the plateau occurs at $d/R_0 \simeq 1.3$. For larger offsets, the sheet can be assumed to remain in the plane of the substrate [Fig. 3, inset (a)]. When $d/R_0 < 1.3$ [Fig. 3, inset (b)], the deformation of the drop at initial crush brings part of the liquid beyond the edge.

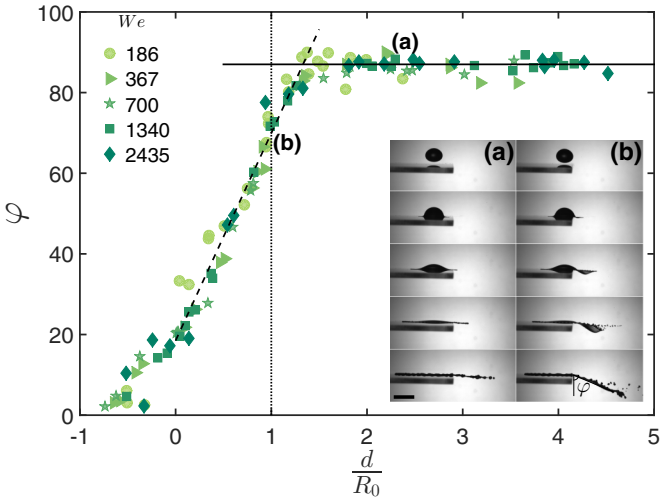

FIG. 3. Inclination φ of the sheet with respect to the vertical as a function of the offset d/R_0 for different We (see Table I for symbols of We). The solid line is $\varphi = 87^\circ$ and the dashed line represents Eq. (1). The inset shows the side-view time sequence of a drop impacting near an edge at We = 680 for (a) $d/R_0 = 2.2$ and (b) $d/R_0 = 1$. Images are taken at -0.2, 0.4, 1, 2.2, and 6.4 ms from the time of impact, respectively, from top to bottom. The scale bar is 4 mm.

This creates a bulge and jeopardizes a planar sheet expansion. The bulge, however, resorbs during the retraction and the sheet becomes planar again, but inclined. In the remainder of this paper, we exclude experiments with $d/R_0 < 1$, for which drops are split by the edge.

Both the shape and the amount of liquid in the sheet vary with the offset. Figure 4 shows four impacts with the same We but different d/R_0. The initial spreading on the solid is obviously identical for all, and almost axisymmetric. With a smaller offset, the liquid reaches the edge and enters the air sooner and consequently at higher speed. The extension of the sheet in the air is faster than that on the solid in the perpendicular direction while it follows the extension speed of the solid tangentially to the edge. This anisotropy in extension causes a distortion of the sheet that is more pronounced as the offset decreases. The maximal extensions of the sheet in directions normal and tangential to the edge are reached at different times, which strongly conditions the subsequent retraction. The rim at the front of the sheet becomes more corrugated and emits droplets sooner than the rim close to the edge [Fig. 4(b)].

As offset is varied, three main scenarios with increasing asymmetry emerge.

Scenario I. When d is sufficiently large (Fig. 4, row 1), the maximum extension of the sheet is reached simultaneously along and normal to the edge. The shape of the sheet is approximately axisymmetric, analogous to spreading on the solid. The sheet retraction is also axisymmetric. Droplets are only emitted during this retraction phase.

Scenario II. As d decreases (Fig. 4, rows 2 and 3), the maximum extension is both larger and reached later in the direction normal to the edge than tangent to the edge. The retraction of the sheet is mostly dominated by the early motion tangent to the edge. The final shape prior to collapse varies from a small triangle attached to the edge to a rectangle with a width along the edge smaller than its length normal to it. The sheet collapses all at once into a filament [Figs. 4(e), rows 2 and 3, and 4(f), row 3]. The breakup of this filament generates droplets that are significantly smaller than those ejected from the sheet.

Scenario III. Finally, at $d/R_0 \sim 1.3$ (Fig. 4, row 4), the sheet anisotropy is so pronounced that it takes a polygonal shape that is conserved during retraction. The retraction along the edge is completed, while it has only started in the perpendicular direction. The sheet then pinches and separates from the edge before collapse. This pinching also generates a filament that breaks up into tiny droplets.

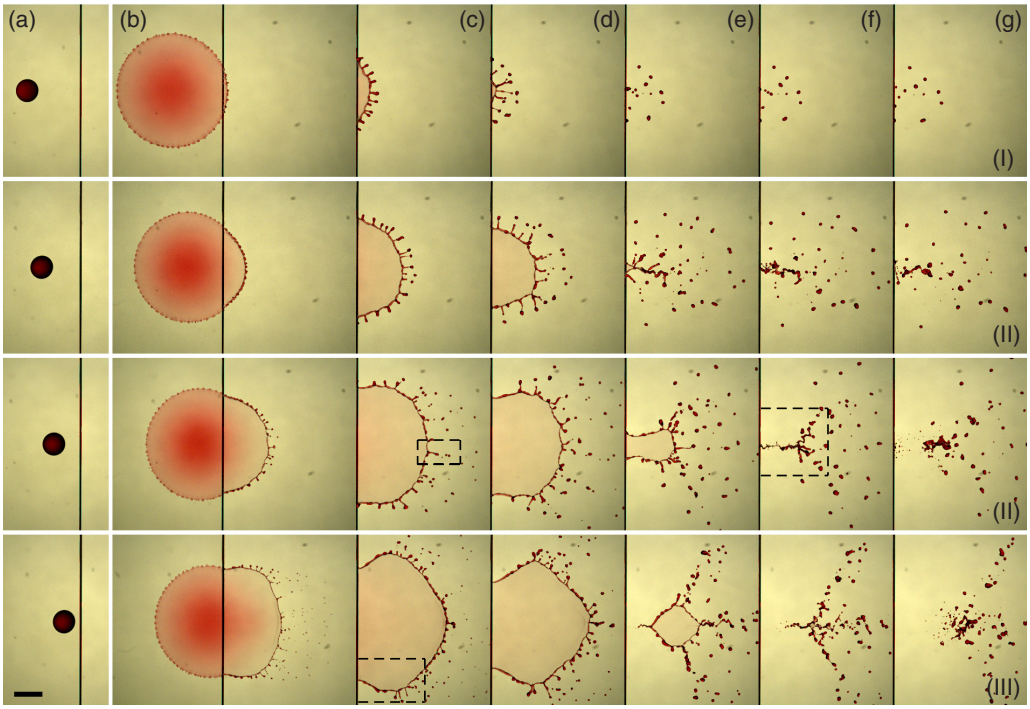

FIG. 4. Time evolution of the sheet in the air for $d/R_0 = 4.4$, 3.2, 2, and 1.3 (top to bottom) and We $= 1340$. Rows 1, 2, 3, and 4 correspond to the retraction scenarios I, II, II, and III, respectively. Snapshots in the same column are taken at the same time t post impact, with $t = 0$, 3, 6, 8, 11, 12, and 14 ms from left to right. Column (a) illustrates the position of the drops right before impact, with respect to the edge. The scale bar is 5 mm. The dashed frames highlight three different droplet ejection mechanisms illustrated in Fig. 16. See videos 1–4 in the Supplemental Material in Ref. [61].

For a given offset, a variation of the impact speed (and corresponding Weber number) does not strongly modify the shape of the liquid sheet. Three examples of impacts taken at identical $d/R_0 \simeq 1.3$ and different speeds are illustrated in Fig. 5, all leading to scenario III. Differences are nevertheless observed, in terms of both temporal evolution and size of the sheet. At higher impact speed, the maximal sheet expansion is larger, but collapses sooner. The ejected droplets are also smaller and are ejected sooner.

IV. SHEET DYNAMICS

The scenarios discussed in Sec. III are first summarized in an offset vs Weber diagram (Fig. 6). For We $\lesssim 186$, only the axisymmetric scenario I subsists for $d/R_0 \geqslant 1.3$.

The sheet kinematics is quantified through the evolution of its extension $l_n(t)$ [$l_t(t)$] in the direction normal to the edge (tangential to the edge), as illustrated in Fig. 7. We also measured the spreading $R_s(t)$ of the liquid on the solid, since this motion is a prerequisite to the expansion of the sheet in the air. These measurements are performed automatically with custom image processing in IMAGEJ and MATLAB. By convention, times are measured from time of impact.

A. Spreading on a solid

Upon impact, the spreading radius $R_s(t)$ quickly increases and reaches a maximum R_{sM} in a finite time t_{sM} [Fig. 8(a)]. Slight dewetting is then observed, due to the weak hydrophilicity of the

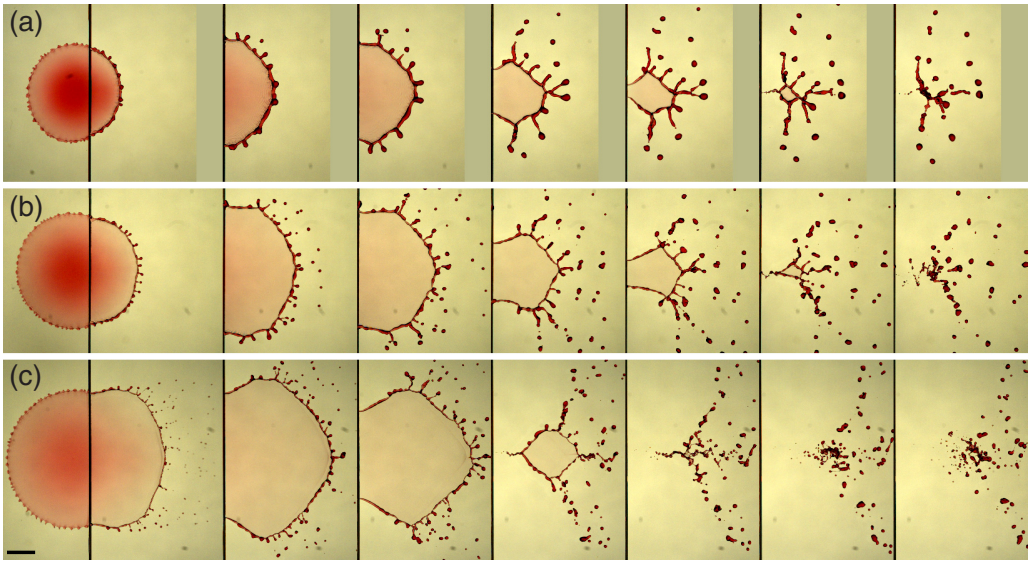

FIG. 5. Time evolution of the sheet in the air for We = 367, 700, and 1340, from top to bottom, for $d/R_0 =$ 1.3, all leading to scenario III. Snapshots in the same column are taken at the same time t post impact, with $t = 3$, 6, 8, 11, 12, 13, and 14 ms from left to right. The scale bar is 5 mm. See videos 4–6 in the Supplemental Material in Ref. [61].

substrate [62]. At first order the expansion dynamics on the solid is not affected by the fact that part of the sheet is then expanding in air. Indeed, the shape of the liquid rim on a solid remains circular and centered on the impact point, during the whole expansion and independently of the offset d [Figs. 8(a) and 8(b)]. During the retraction, we observe capillary waves emitted by the dewetting dynamics, parallel to the edge, similar to the ones observed along the rim, on the solid, away from

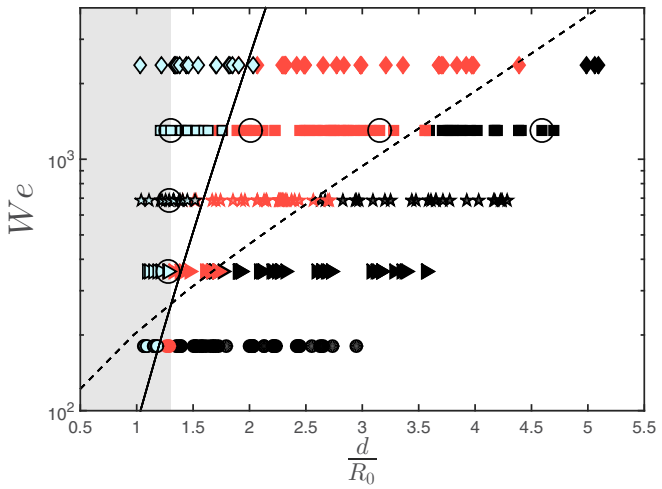

FIG. 6. Phase diagram We vs d/R_0, in which different sheet asymmetry scenarios are colored differently: I, black; II, red (gray); and III, blue (clear). Symbols correspond to different We, according to Table I. The data corresponding to the examples of Figs. 4 and 5 are circled. The shaded region $d/R_0 < 1.3$ corresponds to experiments for which the sheet is not planar. The solid and dashed lines correspond to Eqs. (15) and (16), respectively.

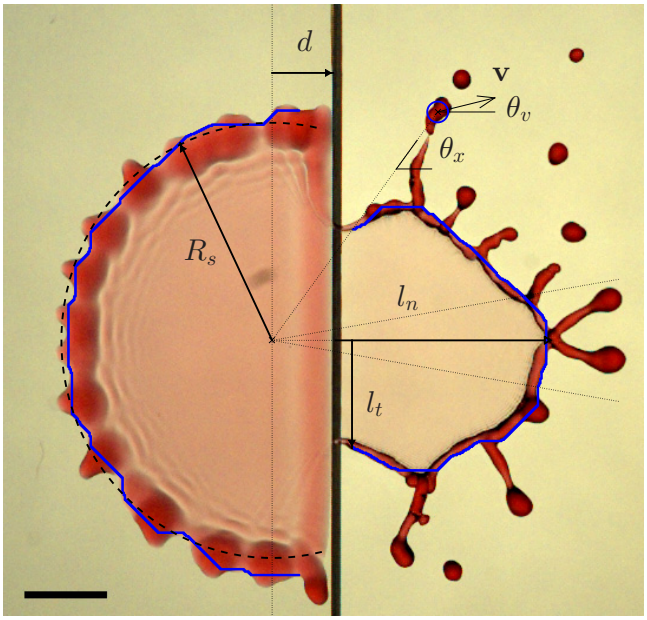

FIG. 7. Main variables that characterize the kinematics of the spreading on a solid, of a liquid sheet in the air, and of ejected droplets. The contours (blue lines) are detected by image processing, after thresholding and morphological removal of the corrugations. This particular image is taken 10.5 ms after impact, at offset $d/R_0 = 1.28$ and $\mathrm{We} = 367$. The scale bar is 4 mm. The radius R_s of the spreading liquid on the solid, the extension of the liquid sheet tangent to the edge l_t, and the normal extension of the sheet l_n are represented. The latter is taken to be the quantile 85% in distance to the edge of the contour of the sheet located in a sector of $\pm 10^\circ$ (fine dotted lines). Several properties are recorded for each droplet at the time they separate from the sheet: the angular position θ_x (measured from the impact point), the radius r of a sphere of equivalent volume (here circled in blue), and the magnitude v and direction θ_v of the ejection velocity $\mathbf{v}$.

the edge [Figs. 2(e) and 2(f)]. They seem to indicate a separation between on-solid and in-the-air dynamics. A traveling wave along the edge following the retraction of the sheet in the air is also visible, but its effects appear to be localized close to the edge. Previous analysis of the early time of spreading suggests that the spreading radius $R_s(t)$ increases proportionally to $\sqrt{t}$ [62]. This scaling law can be understood by considering a circle that moves at constant speed towards a straight line. From a purely kinematic point of view, as soon as the circle intercepts the line, the corresponding chord length grows as the square root of the time from interception. However, at later times the spreading dynamics involves several dissipation mechanisms and there is no simple model that fully describes its kinematics [62–66]. Consequently, we chose to fit an empirical function $R_s(t)$ that grows as $\sqrt{t}$ in the early times and saturates in a finite time

$$\frac{R_s(t)}{R_{sM}} \simeq \sqrt{\frac{t}{t_{sM}}\left(2 - \frac{t}{t_{sM}}\right)}. \tag{2}$$

This expression is only valid for $t \leqslant t_{sM}$. Both R_{sM} and t_{sM} are obtained by least-squares fitting for each individual impact.

The observed maximum spreading R_{sM} increases with We [Fig. 8(a), left inset]. This variation is well captured by the empirical law of [67],

$$\frac{R_{sM}}{R_0} = \frac{\mathrm{We}^{1/2}}{1.14 + \mathrm{We}^{2/5}\mathrm{Oh}^{1/5}}, \tag{3}$$

where the constant 1.14 is fitted on our data.

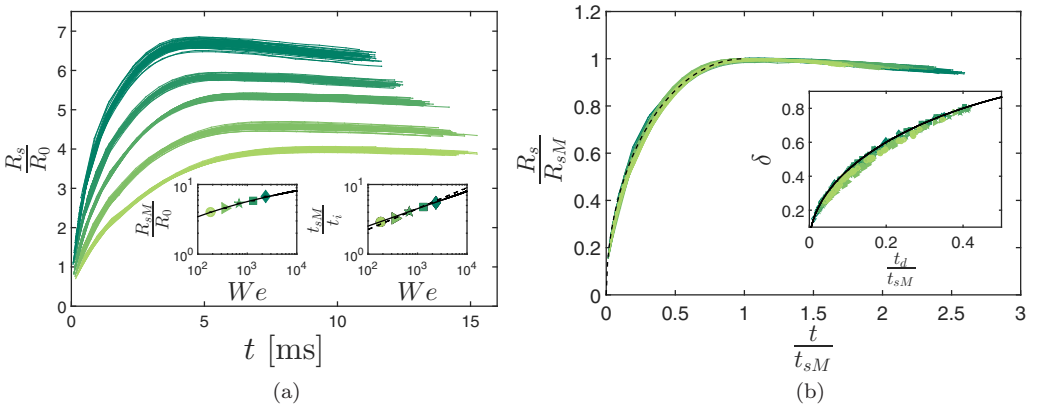

FIG. 8. (a) Time evolution of the spreading radius R_s/R_0 for increasing We (from bottom to top, We = 186, 367, 700, 1340, and 2435). The left inset shows the maximum spreading R_{sM}/R_0 as a function of We. The solid line corresponds to Eq. (3). The right inset shows the time t_{sM}/t_i of the maximum spreading as a function of We. The solid line corresponds to Eq. (4). The dashed line is the scaling $t_{sM}/t_i \simeq \mathrm{We}^{3/10}\mathrm{Oh}^{-1/10}$ from [68]. (b) Rescaled time evolution of the spreading radius R_s/R_{sM} vs t/t_{sM}, for the five We values in Table I. The dashed line shows Eq. (2). The inset shows dimensionless offset $\delta = d/R_{sM}$ as a function of t_d/t_{sM}. The solid line corresponds to Eq. (5). Symbols correspond to different We, all collapsed from 186 to 2435.

The time at which the spreading radius reaches its maximum also increases with We [Fig. 8(a), right inset]. It can be adjusted with the power law

$$t_{sM} \sim \mathrm{We}^{1/4} t_i, \tag{4}$$

with $t_{sM} = 0.8\,\mathrm{We}^{1/4} t_i$, where 0.8 is fitted and $t_i = 2R_0/V_0$ is the impact time (Table I). The exponent 1/4 suggests that the time of maximum spreading is almost inversely proportional to $\sqrt{V_0}$, as observed in Ref. [30]. The alternative $t_{sM} \simeq 0.3\,\mathrm{We}^{3/10}\mathrm{Oh}^{-1/10}$ proposed in Ref. [68] is also in good agreement with our data.

The normalized spreading radius R_s/R_{sM} as a function of the normalized time t/t_{sM} is shown in Fig. 8(b). Data from different We collapse onto a single curve, which is very well approximated by Eq. (2) for $t < t_{sM}$. The match between the experimental curves and the equations is not valid beyond $t > t_{sM}$ as dewetting obeys a different dynamics that is sensitive to the surface properties of the substrate. From Eq. (2) we can predict the time t_d at which the liquid arrives at the edge of the substrate [$R_s(t_d) = d$],

$$\frac{t_d}{t_{sM}} = 1 - \sqrt{1-\delta^2}, \tag{5}$$

where $\delta = d/R_{sM} < 1$ is defined as the dimensionless offset. This equation is also in good agreement with the experimental measurements of the time of formation of the liquid sheet [Fig. 8(b), inset].

B. Expansion and retraction of the liquid sheet in the air, normal to the edge

As soon as it takes off from the edge, the liquid is not subjected anymore to the surface shear dissipation. We describe the extension of the sheet normal to the edge $l_n(t)$ by defining a dimensionless time

$$\tau_n = \frac{t - t_d}{t_{nM} - t_d} \tag{6}$$

from fluid entry in the air $t - t_d$, divided by the time $t_{nM} - t_d$ of maximum extension in the air, normal to the edge. Similarly, the normal extension of the sheet is normalized by its maximal extension l_{nM}.

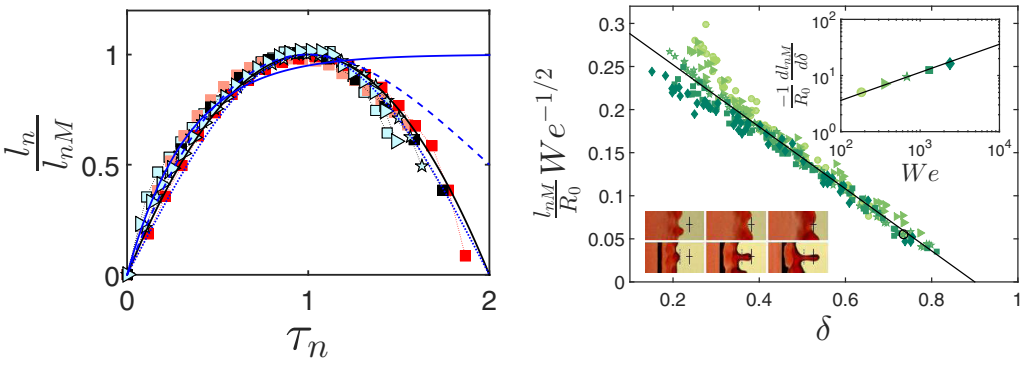

FIG. 9. (a) Normalized time evolution of the sheet extension normal to the edge $l_n(t)$ for the six examples of Figs. 4 and 5. The colors represent the different scenarios corresponding to these examples: I, black; II, light and dark red (light and dark gray); and III, blue (clear). The solid black line is Eq. (7). The blue lines correspond, respectively, to the theoretical results from [38] (solid) and from [39] (dashed) and to a harmonic oscillator suggested in Refs. [69,70] (dotted). (b) Maximum normal extension of the liquid sheet l_{nM} normalized by $R_0 \mathrm{We}^{1/2}$ as a function of δ. The solid line shows Eq. (8), which is fitted on all the data points (with $d/R_0 > 1.3$). The values for different We are 186 (◯), 367 (▷), 700 (★), 1340 (□), and 2435 (◇). The top inset shows the slope l_{nM}/R_0 vs δ, as a function of We. The bottom inset shows the late spreading on solid, close to reaching R_{sM}, with and without the presence of an edge (bottom and top lines, respectively), for $\delta = 0.73$ and $\mathrm{We} = 180$ (black circle in the main graph). The time interval is 1.5 ms from $t = 5$ ms after impact until reaching R_{sM}, from left to right. The cross and the dotted line are positioned at distances R_{sM} and $l_{nM} + d$ from the impact point, respectively. The cross height is 1 mm.

With this normalization, all experimental data collapse onto a single curve

$$\frac{l_n}{l_{nM}} = \tau_n(2 - \tau_n), \tag{7}$$

as shown in Fig. 9(a). Interestingly, this shows that the acceleration of the sheet normal to the edge is approximately constant during extension and retraction. Our results were also compared to previous theoretical work on axisymmetric sheet expansion. The theoretical relations in Refs. [38,39] for the expansion of axisymmetric liquid sheets, once rescaled, show relatively good agreement with our experimental data during the expansion of the sheet, but not during its retraction. The experimental data are better captured by a simple harmonic oscillator in the form $l_n/l_{nM} = \sin(\pi\tau_n/2)$, as suggested in Refs. [69,70].

Both l_{nM} and t_{nM} are obtained for each experiment by least-squares fitting Eq. (7) for each impact. The normal extension is expected to depend both on We and on the history of the liquid on the surface prior to reaching the edge [42]. To investigate this latter dependence, the maximum normal extension l_{nM} is shown as a function of the dimensionless offset δ in Fig. 9(b). A linear decrease of l_{nM} with δ is observed,

$$\frac{l_{nM}}{R_0} = 0.36\sqrt{\mathrm{We}}(0.9 - \delta) \tag{8}$$

$$\simeq 0.44\frac{V_0 t_c}{R_0}(0.9 - \delta), \tag{9}$$

where the coefficients 0.36 and 0.9 are obtained from the best fit and $t_c = \sqrt{4\rho R_0^3/(3\sigma)}$ is the capillary time (Table I). The coefficient 0.9 in Eq. (8) indicates that $l_{nM} = 0$ for $\delta = 0.9 < 1$. This is counterintuitive, as it suggests that on the solid, away from the edge, the spreading is slightly larger (by 10%) despite surface shear. However, corrugations around the sheet form earlier when it is in the

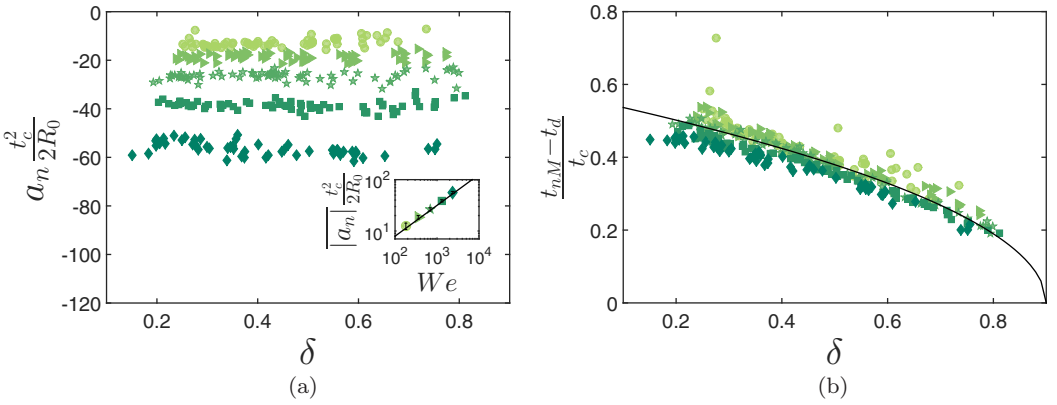

FIG. 10. (a) Nondimensional acceleration a_n of the sheet normal to the edge as a function of offset δ. The inset shows the absolute value of a_n, averaged over δ, as a function of We. The solid line is Eq. (10). (b) Normalized time of maximum normal extension $(t_{nM} - t_d)/t_c$ as a function of the offset δ. The solid line corresponds to Eq. (11). The values of We are 186 (◯), 367 (▷), 700 (★), 1340 (□), and 2435 (◇).

air than when it is spreading on the solid. This could be due to the larger deceleration experienced by the sheet in the air than on the solid. Since our measurement of the sheet extension does not include such corrugations, $l_{nM} = 0$ for $\delta = 0.9$.

The acceleration of the sheet in the air normal to the edge is obtained by differentiating Eq. (7) twice: $a_n = -2l_{nM}/(t_{nM} - t_d)^2$. Figure 10(a) shows that a_n, scaled by $2R_0/t_c^2$, is independent of the offset δ. Its average $\overline{a_n}$ over the full range of δ follows a power law in We:

$$\overline{a_n}\frac{t_c^2}{2R_0} = -0.5\,\mathrm{We}^{0.6}, \tag{10}$$

where the coefficient 0.5 and the exponent 0.6 are fitted. These dependences suggest that $\overline{a_n}$ is slightly higher than V_0/t_c.

The time $t_{nM} - t_d$ needed to reach maximum sheet extension is deduced from Eqs. (8) and (10). The ratio gives a dependence on $\mathrm{We}^{-0.05}$, negligible at first order. In dimensionless form

$$\frac{t_{nM} - t_d}{t_c} \simeq 0.6\sqrt{0.9 - \delta}, \tag{11}$$

where 0.6 is fitted. This result matches the experimental data well [Fig. 10(b)]. In summary, the kinematics of the sheet extension normal to the edge as a function of We and δ is well captured by the combination of Eqs. (7), (9), and (11).

C. Comparison to the radial extension in axisymmetric impact configurations

The impact near an edge involves spreading on a solid followed by expansion in the air, an intermediate between two axisymmetric configurations already investigated: an impact on an infinite solid [20,67] and a centered impact on a circular target of size comparable to the drop [38,39,42] [Fig. 11(a)]. In order to compare the maximum distance reached by the liquid in these three configurations, we performed additional experiments of impacts on a pole. The pole radius d corresponds to the distance the liquid travels on the solid before taking off, so it is equivalent to the offset d defined for the impact near an edge. We considered two ratios of the pole to drop size $d/R_0 \in \{1.5, 2.4\}$ and three Weber numbers $\mathrm{We} \in \{370, 700, 1340\}$. The substrate material and the impacting drop (size and composition) are the same as for the edge configuration. Figure 11(b) compares prior models of sheet extension: (i) the maximum spreading radius on a solid R_{sM} from [67] [Eq. (3)] and (ii) the maximum radial extension of the liquid sheet (from impact point)

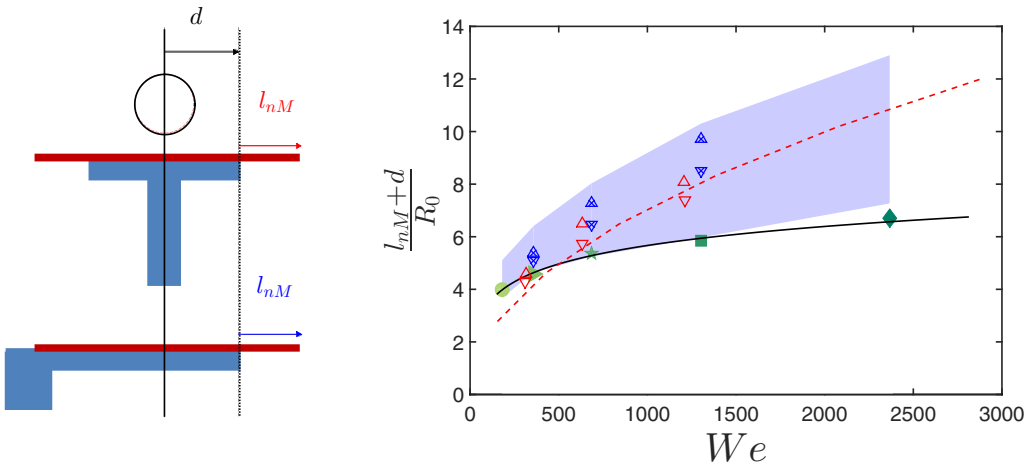

FIG. 11. (a) Schematics of the geometrical similarity between the sheet extension for the edge and pole configurations. (b) Comparison of the maximum radial distance from the impact point reached by the liquid for three configurations: full spreading on a solid (closed green symbols, R_{sM}/R_0), liquid sheet from a flat edge [shaded area, $(l_{nM}+d)/R_0$], and liquid sheet from a pole [open triangles, $(l_{nM}+d)/R_0$]. Two ratios of the pole to drop radius were considered: $d/R_0 = 1.5$ ($\triangle$) and $d/R_0 = 2.4$ ($\triangledown$). The crossed $\triangledown$ and $\triangle$ represent the maximal distance reached in edge experiments with the same offsets d/R_0. The solid and dashed lines correspond to Eqs. (3) and (12), respectively.

from [38,40],

$$\frac{l_{nM}+d}{R_0} \simeq \sqrt{\mathrm{We}}, \tag{12}$$

with a prefactor 0.22 in Eq. (12) corresponding to the rounded average between the prefactor 0.227 for $d/R_0 \in \{1, 1.4\}$ in Ref. [38] and the prefactor 0.22 for $d/R_0 = 1.67$ in Ref. [40]. Equation (12) is in good agreement with our experimental data on the pole. The power law $l_{nM} \sim \mathrm{We}^{1/2}$ [Eq. (8)] for the edge is similar to the dependence on $\sqrt{\mathrm{We}}$ of Eq. (12) obtained for the pole [38–40].

Figure 11(b) shows that the liquid sheet for large We and small offsets goes further than the liquid only spreading on the solid. Indeed, spreading on a solid dissipates energy through viscous friction well captured by a Blasius-type boundary layer [42], which reduces liquid spreading. The experimental values of R_{sM} are in good agreement with Eq. (3). More surprisingly, the maximal distance reached by the liquid sheet is always higher with a straight edge than with a circular edge at the same distance d/R_0 from impact point. This is counterintuitive since in all directions not normal to the straight edge, the liquid spreads more than d on the solid prior to taking off from the edge. By contrast, in the pole configuration, the liquid sheet forms at the same time after the same spreading distance d in every direction. A possible explanation for this larger distance reached by the sheet from a straight edge is that the rupture of symmetry enables retraction from the back of the sheet leading to further extension normal to the edge.

D. Expansion and retraction of the liquid sheet in air, along the edge

We proceed by rationalizing the time evolution of the liquid sheet in the vicinity of the edge. As can be seen in Figs. 2(b)–2(d), the extension of the sheet along the edge initially closely follows the spreading on the solid during the expansion phase. By contrast, dewetting on the solid is much slower than the retraction of the sheet along the edge. This tangential extension should therefore be geometrically related to the spreading law $R_s(t)$ through $l_t(t) = \sqrt{R_s(t)^2 - d^2}$. Combining this

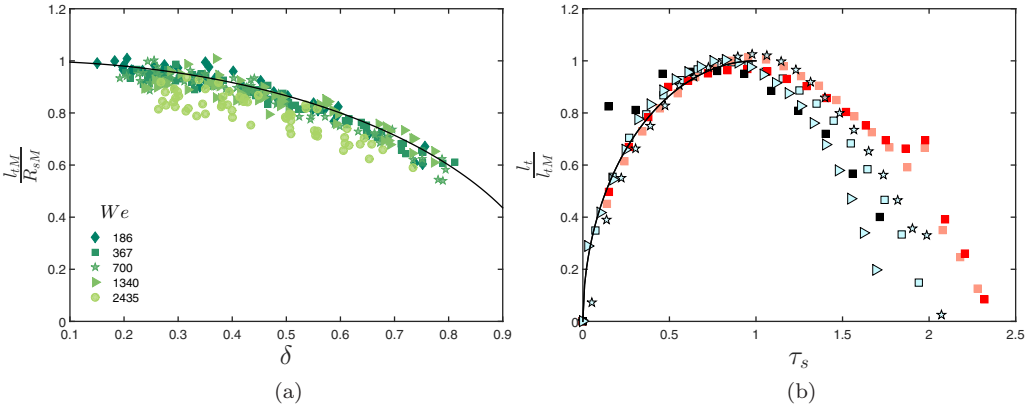

FIG. 12. (a) Maximum tangential extension l_{tM} of the liquid sheet along the edge normalized by the maximum spreading on solid R_{sM}, as a function of offset δ. The solid line is $\sqrt{1-\delta^2}$, in agreement with Eq. (14). (b) Time evolution of the sheet extension along the edge $l_t(t)$, normalized by its maximum value l_{tM} for the six examples of Figs. 4 and 5. The scenarios are represented as follows: I, black; II, light and dark red (light and dark gray); and III, blue (clear). The solid line for $\tau_s < 1$ represents Eq. (13). The values of We are 186 (◯), 367 (▷), 700 (★), 1340 (□), and 2435 (◇).

equation with Eqs. (2) and (5) yields

$$l_t(t) = R_{sM}\sqrt{1-\delta^2}\sqrt{\tau_s(2-\tau_s)} \quad \text{with} \quad \tau_s = \frac{t-t_d}{t_{sM}-t_d}. \tag{13}$$

Again, this square root of time can be interpreted as a kinematic signature of a circle (the sheet) intercepting a straight line (the edge). By identification of Eqs. (2) and (13), we infer that

$$l_{tM} = R_{sM}\sqrt{1-\delta^2}. \tag{14}$$

This prediction is fairly well verified by the experimental measurements of the maximum tangential extension in Fig. 12(a).

In Fig. 12(b), the extension $l_t(t)$ tangent to the edge is represented for the six examples of Figs. 4 and 5, normalized by its maximum value l_{tM} and plotted as a function of τ_s. Due to this normalization, data from these different experiments collapse well onto the curve of Eq. (13) during the expansion phase ($\tau_s < 1$). However, data from different offsets δ diverge from each other during the retraction phase ($\tau_s > 1$). This scattering of the retraction kinematics along the edge may be linked to the uncontrolled dewetting on this flat vertical edge.

Finally, the time at which the sheet collapses along the edge is defined as $t_r - t_d$. This time is different from the full collapse of the liquid sheet only for the experiments of scenario III. This collapse time normalized by the time of maximum normal extension is defined as $\tau_r = (t_r - t_d)/(t_{nM} - t_d)$ and is illustrated in Fig. 13. It increases from $\tau_r \simeq 1.3$ at low δ and then saturates at $\tau_r \simeq 2$ at large δ. It is only slightly dependent on We for intermediate δ. Its average value is $\tau_r = 1.76$, with a standard deviation of 0.2.

E. Asymmetry and sheet envelope

In Fig. 4, we observed three qualitatively different scenarios of sheet expansion and retraction. Each scenario is observed in a given region of the diagram (We, d/R_0) in Fig. 6. Boundaries between these regions are nontrivial. The preceding investigation of the sheet kinematics highlighted the importance of the dimensionless offset $\delta = d/R_{sM}$. Moreover, a key difference between the scenarios is the relative asymmetry of the sheet, which could be represented by the ratio l_{nM}/l_{tM}. The separation of scenarios appears more clearly in the diagram ($\delta, l_{nM}/l_{tM}$) of Fig. 14. With this representation,

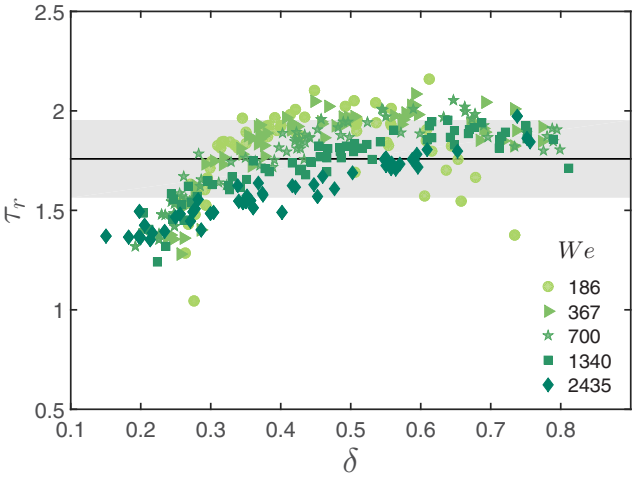

FIG. 13. Normalized time of collapse $\tau_r = (t_r - t_d)/(t_{nM} - t_d)$ of the liquid sheet along the edge as a function of the offset δ. Symbols corresponds to We in Table I. The solid line is the average across We and δ and the gray area corresponds to one standard deviation.

the transition from scenario III to II occurs approximately at

$$\delta = 0.3 \tag{15}$$

and the transition from scenario I to II at

$$\frac{l_{nM}}{l_{tM}} = 0.85. \tag{16}$$

The distance traveled by the liquid spreading on the solid strongly influences the subsequent shape of the liquid sheet in the air. Based on this observation, we propose a first-order model to reconstruct

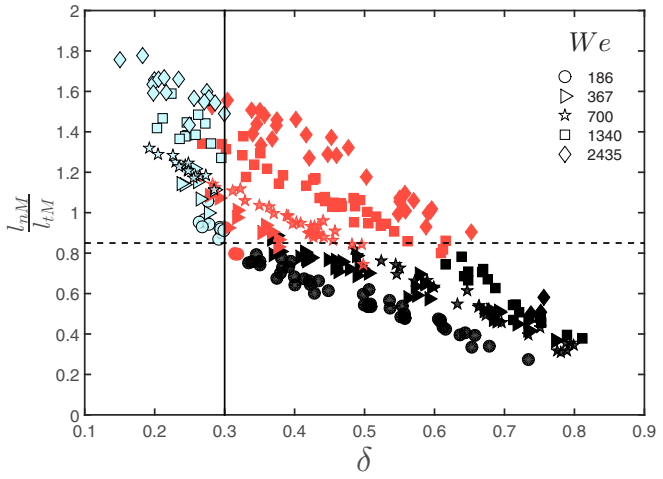

FIG. 14. Scenarios of liquid sheet expansion and retraction, in a $(\delta, l_{nM}/l_{tM})$ diagram. The symbols correspond to different We given in Table I and the colors to different scenarios: I, black; II, red (gray); and III, blue (clear). The solid and dashed lines correspond to Eqs. (15) and (16), respectively. The horizontal line is $l_{nM}/l_{tM} = 0.85$ and the vertical line is $\delta = 0.3$.

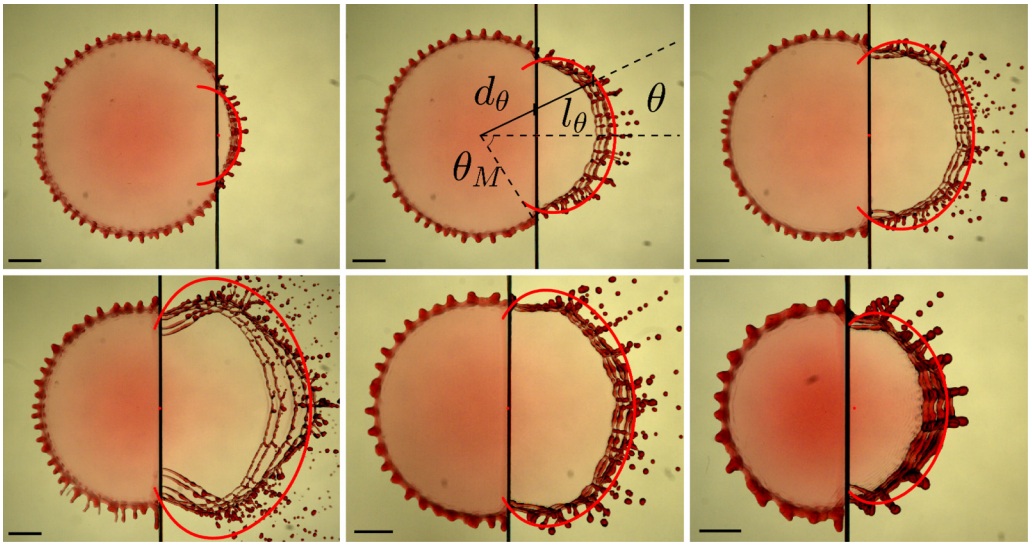

FIG. 15. Time superposition of snapshots from a given experiment, with $t \in [t_{sM}, t_{nM}]$. The curved red solid lines represent the reconstructed envelope region accessible to the sheet, predicted by Eq. (17). The top row shows, from left to right, We = 1340 and $\delta = 0.79$, 0.54, and 0.34. The bottom row shows, from left to right, We = 1340, 700, and 367 and $d/R_0 = 1.3$, with $\delta = 0.22$, 0.24, and 0.28. Scale bars are 4 mm.

the maximal region accessible to the expanding sheet. On the solid, the liquid spreads radially from the impact point and reaches the edge after a distance $d_\theta = d/\cos\theta$, where θ is the angular position from the impact point, measured from the symmetry axis (Figs. 7 and 15). Since d_θ is bounded by R_{sM}, θ must be smaller than $\theta_M = \cos^{-1}\delta$. By replacing d by d_θ (or equivalently δ by $\delta/\cos\theta$) in Eq. (8), we obtain a prediction of the maximum extension l_θ reached by the sheet in the θ direction from the normal to the edge:

$$\frac{l_\theta}{R_0} = 0.36\sqrt{\mathrm{We}}\left(0.9 - \frac{\delta}{\cos\theta}\right). \tag{17}$$

Since the time of maximum extension varies with the direction considered (i.e., $t_{nM} \neq t_{sM}$), Eq. (17) does not predict the shape of the sheet at a given instant. It rather gives the envelope accessible to the sheet during its expansion, as shown in Fig. 15 for various We and δ. Equation (17) captures well the sheet's outer envelope and only overestimates that envelope for the largest We and smallest d (bottom left picture in Fig. 15) that corresponds to scenario III. In that particular case, the time of the maximum normal distance to the edge occurs much later than the tangential one which depends on the details of pinning and contact line not captured by Eq. (17). This could be extended to a full model accounting for a differential dissipation for fluid parcels at the surface, which effectively experience different cumulative viscous dissipation, shown to be well captured by a Blasius-type boundary layer, even in this transient impact dynamics on average wetting surface [42].

V. DROPLET EJECTION

In this section, we characterize the ejected droplets from a statistical point of view and we relate their properties to the asymmetric kinematics of the sheet. We first discuss the mechanisms and direction of ejection and then the initial speed and mass to rationalize their traveled distance. Finally, we take a look at the number of ejected droplets and summarize the effect of sheet asymmetry on the droplet size distributions. More details on droplet tracking and mass estimation are provided in Appendix A.

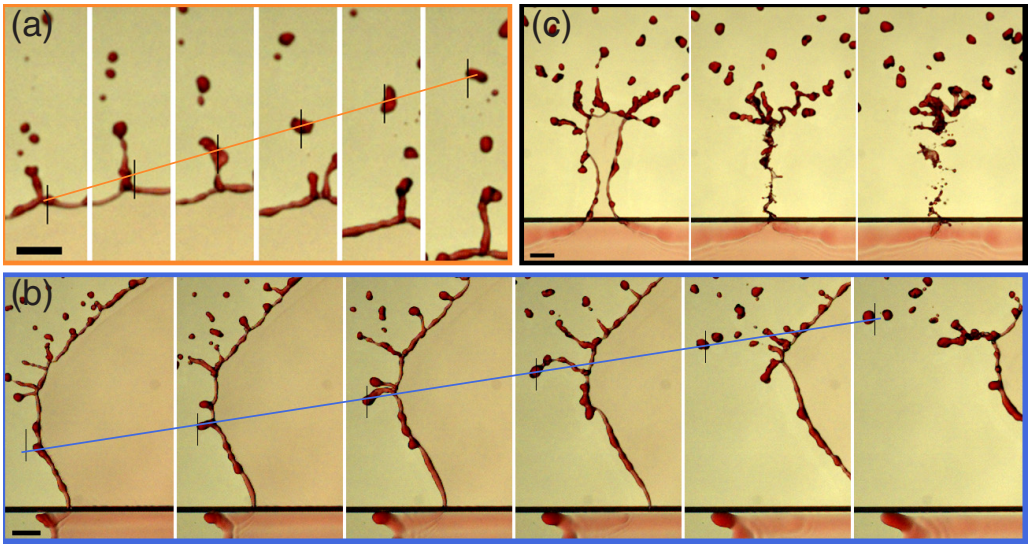

FIG. 16. Mechanisms of droplet ejection. (a) Radial ejection from the rim. Successive snapshots are separated by 0.4 ms, from 6.2 ms after impact. The highlighted droplet is ejected at $\tau_n = 1.02$, with a mass $m = 0.23$ mg and a speed $v = 0.28V_0$. Its ejection angles are $\theta_x = 4^\circ$ and $\theta_v = -9^\circ$. (b) Tangential ejection from the rim. Successive snapshots are separated by 0.6 ms, from 4 ms after impact. The highlighted droplet is ejected at $\tau_n = 1.17$, with a mass $m = 0.29$ mg and a speed $v = 0.46V_0$. Its ejection angles are $\theta_x = 48^\circ$ and $\theta_v = 7^\circ$. (c) Collapse of the sheet. Snapshots are taken at 11.8, 12.2, and 13 ms after impact. Scale bars are 2 mm. The orange and blue solid lines join the center of mass of the ejected droplets across frames. The vertical black lines are at fixed position, so they highlight the left-to-right motion of the droplets. These three snapshots correspond to close-up of the droplet ejections framed in Fig. 4. Panels (b) and (c) display also a small part of the solid substrate. The edge is then the horizontal black line.

A. Ejection mechanisms and direction of ejection

Three ejection mechanisms are identified and illustrated in Fig. 16. They are differentiated according to the time, position, and directionality of the droplet ejections (Fig. 17). The selected snapshots correspond to parts of the movies illustrated in Fig. 4.

(i) The first mechanism is called radial ejection [Fig. 16(a)]. It concerns droplets from the rim of the expanding sheet (i.e., before sheet collapse), for which the ejection direction θ_v is closely aligned on the radial position from the impact point θ_x (definition in Fig. 7). Each droplet originates from a corrugation along the rim. This corrugation grows in a radial ligament (almost normal to the sheet). The filament then destabilizes into one or several droplets that are ejected perpendicularly to the rim. The droplets mostly inherit the normal velocity that the sheet had during the early growth of the corrugations. They also inherit a small velocity tangent to the rim, which corresponds to a slight lateral displacement of the ligament.

(ii) The second mechanism is called tangential ejection [Fig. 16(b)] and it again concerns droplets ejected from the rim of the sheet. In this case, the ejection direction θ_v is not aligned anymore with the radial position θ_x. This mechanism mostly appears on the sides of the sheet in the most asymmetric scenarios, i.e., II and III. Owing to inertia, the corrugations in which liquid accumulates travel along the rim, away from the edge. When the rim retracts tangentially to the edge, these corrugations destabilize into droplets. However, the velocity inherited by the droplets now mostly comes from the motion of the corrugations along the rim and not from the velocity of the sheet. Consequently, these droplets are ejected in a direction almost parallel to the rim and perpendicular to its retraction velocity. As the capillary force from the sheet does not directly oppose the motion of these corrugations, the resulting droplets tend to go faster than the droplets ejected radially. This is illustrated in Fig. 16.

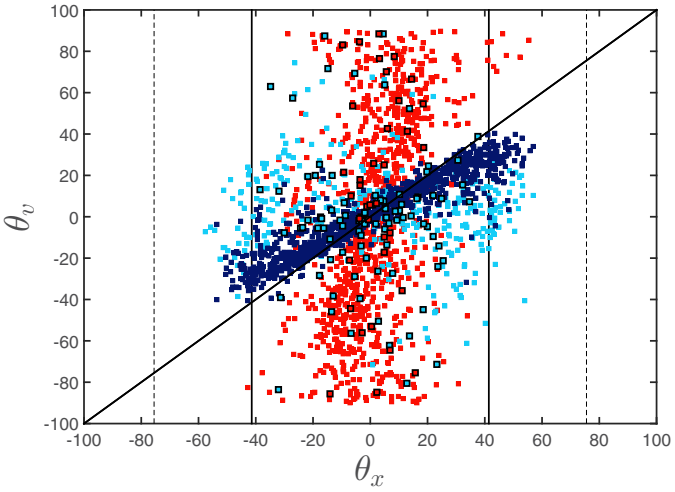

FIG. 17. Angle of the ejection velocity θ_v as a function of the angular position of ejection θ_x measured from the impact point (defined in Fig. 7), for We = 1340. Symbols without (with) black contour correspond to $\delta \in [0.2, 0.3]$ ($\delta \in [0.7, 0.8]$). The color refers to the ejection time: dark blue, during sheet expansion, i.e., $\tau_n < 1$; light blue, during sheet retraction, i.e., $1 < \tau_n < \tau_r$; and red, after sheet collapse, i.e., $\tau_n > \tau_r$. The inclined solid line is the bisector $\theta_v = \theta_x$. The vertical lines correspond to the maximum sheet angle θ_M (defined in Fig. 15), for $\delta = 0.25$ (dotted) and $\delta = 0.75$ (solid).

(iii) The last mechanism occurs when the sheet collapses [Fig. 16(c)]. The resulting liquid filament has a very complex shape and it breaks up in a wide variety of droplets. These droplets may be inherited from the late retraction speed of the sheet. A particular collapse event is present when the sheet retracts in scenarios II and III. The two rims of the sheet near the edge converge quickly towards each other. Their violent collision generates many droplets that are much smaller than those emitted from the first two mechanisms. The direction of ejection can also be out of the plane of the sheet [Figs. 2(g) and 2(h) - side views].

The prevalence of each ejection mechanism is observed in Fig. 17, where the direction θ_v of droplet ejections is plotted against their angular position θ_x. Droplets are distinguished according to the sheet kinematics (expansion, retraction, and collapse) at the moment of their ejection. During sheet expansion ($\tau_n < 1$), most droplets are ejected radially, i.e., with $\theta_v \simeq \theta_x$. Tangential ejections only appear during sheet retraction ($1 < \tau_n < \tau_r$), when the sheet asymmetry is sufficiently developed. At small offset δ, most of them satisfy $|\theta_v| < |\theta_x|$, so their ejection direction is more normal to the edge than a droplet ejected radially from the same position. Droplets ejected from the collapse of the sheet ($\tau_n > \tau_r$) remain localized close to the symmetry axis, in $|\theta_x| \lesssim 20^\circ$. However, their ejection direction θ_v is much more scattered than for other mechanisms.

The radial ejection mechanism was already observed in the axisymmetric configuration of impact on a pole [38,39] and the mass distribution was characterized. The collapse mechanism is also observed in such impacts when the sheet experiences local piercing [38,39]; this typically occurs when the impact is not perfectly centered on the pole. The tangential ejection mechanism and the filament breakup are not present in axisymmetric impacts such as impact on pole.

B. Droplet ejection speed

We now examine how the mechanisms of ejection can affect the speed of the droplets through the asymmetry of the sheet. The speed v at which each droplet is ejected is represented as a function of its ejection time in Fig. 18(a), for the six examples of Figs. 4 and 5. The speed v is naturally normalized by the impact speed V_0, while the time τ_n is normalized by the time of maximum extension of the

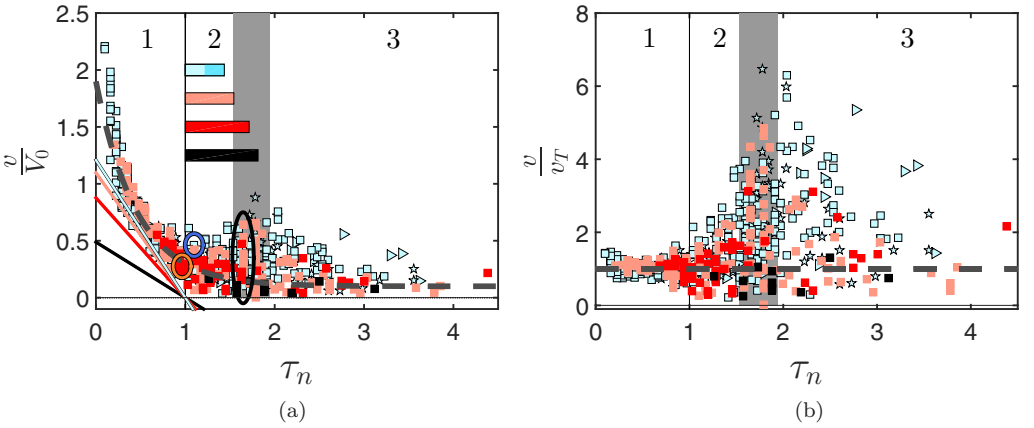

FIG. 18. Time evolution of the droplet ejection speed v normalized by (a) the impact speed V_0 and (b) v_T, for the six examples of Figs. 4 and 5. The time τ_n is normalized according to the normal extension of the sheet. Each data point corresponds to a single droplet. Symbols correspond to the Weber numbers We = 367 (▷), 700 (★), and 1340 (□), while colors indicate the degree of asymmetry from lowest (I) to highest (III) with I, black; II, light and dark red (light and dark gray); and III, blue (clear). The gray area indicates the time τ_r at which the sheet has fully retracted from the edge (average across We and δ, plus or minus the standard deviation). The numbers 1, 2, and 3 indicate periods of time of the sheet (1, sheet expansion; 2, sheet retraction; and 3, after full sheet retraction along the edge). In (a), horizontal rectangles represent the duration of the sheet retraction. The darker blue rectangle in scenario III corresponds to the retraction of the sheet after it has pinched from the edge. The inclined solid lines correspond to Eq. (18) for the six examples (one line per scenario). The dotted line represents Eq. (19). Circled data points correspond to the snapshots of Fig. 16.

sheet normal to the edge. All the data corresponding to normal extension ($\tau_n < 1$) collapse onto a single curve, so v/V_0 is a decreasing function of τ_n only, for all We and δ. The ejection speed becomes more scattered as soon as $\tau_n > 1$, i.e., during the retraction and collapse of the sheet. The time τ_r at which the sheet collapses along the edge also corresponds to a maximum scatter of ejection speed.

The influence of the sheet kinematics on droplet ejection can be better assessed by looking at the speed of the sheet in the direction normal to the edge [derived from Eq. (7)]:

$$\frac{1}{V_0}\frac{dl_n}{dt} = \frac{2l_{nM}}{V_0(t_{nM} - t_d)}(1 - \tau_n) \simeq 1.47\sqrt{0.9 - \delta}(1 - \tau_n). \tag{18}$$

The normal extension speed of the sheet is again proportional to the impact speed V_0 at first order. It is reported in Fig. 18(a), where it sets a lower bound to the droplet ejection speed. Indeed, droplets ejected during the sheet expansion must go faster than the sheet from which they detach.

A careful examination of Fig. 18(a) indicates that, for $\tau_n > 1$, the scattering of ejection speed at a given time depends on the considered scenario. In order to better quantify this scattering, we define the average speed $v_T(\tau_n)$ of all the droplets radially ejected at a given τ_n. These considered droplets are from all scenarios combined when $\tau_n < 1$ and only from scenario I when $\tau_n > 1$. This average velocity is well captured by

$$\frac{v_T}{V_0} = 2.1e^{-2.5\tau_n} + 0.1, \tag{19}$$

as illustrated in Fig. 18(a). The deviations of the ejection speed from v_T are visible in Fig. 18(b).

Data from scenario I align with the curve observed for $\tau_n < 1$, with little scatter. The corresponding droplets are radially ejected, through the same mechanism as all the droplets ejected in $\tau_n < 1$. By contrast, the ejection speed at $\tau_n > 1$ is more scattered for scenarios II and III, which suggests the emergence of tangential ejections. Indeed, the filament breakup occurs in τ_r and coincides with the maximum scatter of data for these scenarios.

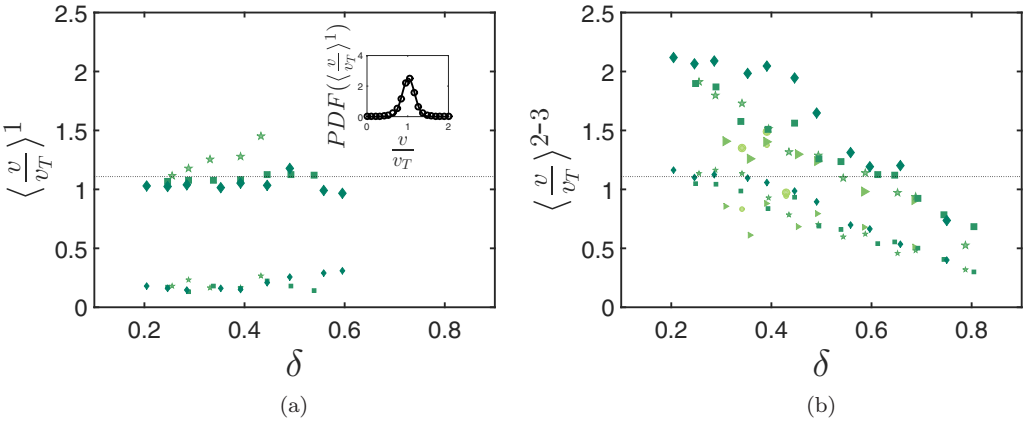

FIG. 19. Average (large symbols) and standard deviation (small symbols) of v/v_T for each (We, δ). (a) Over the sheet expansion ($\tau_n < 1$). The dotted line is the average over all (We, δ). The inset shows the PDF of v/v_T during the sheet expansion. The solid line is a fit with a Gaussian distribution of mean 1.05 and standard deviation 0.2. (b) After sheet expansion ($\tau_n > 1$). The dotted line is the average over all (We, δ) for $\tau_n < 1$. The values of We are 186 (◯), 367 (▷), 700 (★), 1340 (□), and 2435 (◇).

The scatter in ejection speeds can be investigated more systematically through the definition of averages over specific time intervals for all experiments at given (We, δ). These averages are defined for any variable X as follows:

$$\begin{aligned}
\tau_n &< 1 \quad \text{for } \langle X \rangle^1 \text{ (average over sheet expansion)},\\
1 < \tau_n &< \tau_r \quad \text{for } \langle X \rangle^2 \text{ (average over sheet retraction)},\\
\tau_n &> \tau_r \quad \text{for } \langle X \rangle^3 \text{ (average after full sheet retraction from the edge)},\\
\tau_n &> 1 \quad \text{for } \langle X \rangle^{2\text{-}3} \text{ (average after sheet expansion)},\\
\tau_n &> 0 \quad \text{for } \langle X \rangle \text{ (average over all time)}.
\end{aligned} \tag{20}$$

As can be seen in Fig. 19(a), the average speed during sheet expansion is very close to the theoretical speed of radially ejected droplets, i.e., $\langle v/v_T \rangle^1 \sim 1$, for all We and δ, which is expected from the definition of v_T. The corresponding standard deviation is about seven times smaller than the average value, which confirms the good collapse of the data already seen for $\tau_n < 1$ in Fig. 18. Furthermore, the probability distribution function PDF($\langle v/v_T \rangle^1$), which includes all droplets ejected for $\tau_n < 1$, follows a Gaussian distribution of mean 1.05 and standard deviation 0.2 [Fig. 19(a), inset]. During the retraction and collapse of the sheet (so as soon as $\tau_n \gtrsim 1$), both the average $\langle v/v_T \rangle^{2\text{-}3}$ and corresponding standard deviation decrease linearly with increasing δ [Fig. 19(b)]. The larger scatter at small δ can be attributed to the presence of additional ejection mechanisms (namely, the tangential droplets and the filament collapse). There is almost no dependence on We, which indicates that the sheet asymmetry (measured by δ) drives the droplet ejection pattern only during sheet retraction and collapse.

C. Droplet mass

We now focus on the mass of the ejected droplets, which is a key property that also determines the distance traveled. Information concerning mass estimation can be found in Appendix A. The mass m of the ejected droplets is reported as a function of their normalized ejection time τ_n in Fig. 20(a), for the six examples of Figs. 4 and 5. Contrary to the ejection speed v, the mass m varies on more than three orders of magnitude and it is scattered at all time. Nevertheless, viscosity sets a lower bound to the size of ejected droplets. In the context of partial coalescence, the inhibition of inertial liquid breakup by viscosity was observed for Ohnesorge numbers Oh $\gtrsim 0.025$ [71,72]. It here corresponds

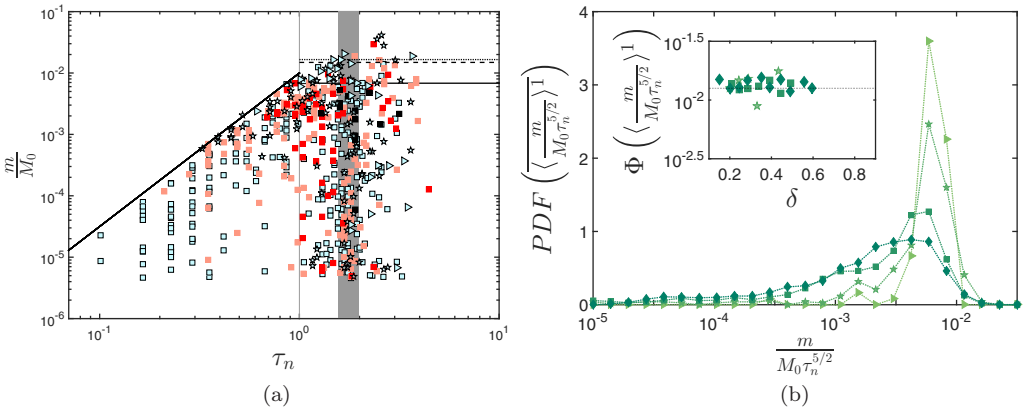

FIG. 20. (a) Time evolution of the mass m of the ejected droplets (normalized by the mass M_0 of the impacting drop) as a function of their normalized time of ejection τ_n, for the six examples of Figs. 4 and 5. Each data point corresponds to a single droplet. Symbols correspond to Weber numbers We = 367 (▷), 700 (★), and 1340 (□), while colors indicate scenarios I, black; II, light and dark red (light and dark gray); and III, blue (clear). The gray area indicates the time τ_r at which the sheet has fully retracted from the edge (average across We and δ, plus or minus the standard deviation). The inclined solid line represents Eq. (21). The horizontal lines correspond to the cutoff mass $\Phi(m/M_0)$ during retraction with We = 367 (dotted), We = 700 (dashed), and We = 1340 (solid). (b) Probability distribution function of the normalized mass $m/(M_0\tau_n^{5/2})$ of droplets ejected during sheet expansion ($\tau_n < 1$), pooled per We (all δ together). The symbols correspond to the values We = 186 (◯), 367 (▷), 700 (★), 1340 (□), and 2435 (◇). The inset shows the saturation value Φ of the PDF, for each We and δ. The dotted line corresponds to the coefficient of Eq. (21).

to a minimum radius of 0.02 mm and a mass $m/M_0 \simeq 5 \times 10^{-7}$. This size is slightly below the resolution of our camera. In addition, m is clearly bounded by a maximal mass that increases with time for $\tau_n < 1$ and saturates to a constant value for $\tau_n > 1$. This maximal droplet mass is still 50 times smaller than the mass $M_0 = 4\pi\rho R_0^3/3$ of the impacting drop.

The increase of this upper bound on mass during sheet expansion ($\tau_n < 1$) seems to be independent of scenario and offset δ and appears to vary as

$$\frac{m}{M_0} \leqslant 0.013\tau_n^{5/2}. \tag{21}$$

Equation (21) suggests that one analyze the statistical distribution of droplet mass, normalized by $\tau_n^{5/2}$ [Fig. 20(b)]. The probability distribution function

$$\mathrm{PDF}\left(\overline{\left\langle\frac{m}{M_0\tau_n^{5/2}}\right\rangle^1}\right)$$

is calculated on all our data, pooled per We (all δ together), which is denoted by a simple overline. This distribution presents a mode that approximately varies as $\mathrm{We}^{-0.2}$, so faster incoming drops generate smaller ejected droplets. There is a cutoff on the right end of this PDF, which corresponds to the maximal mass. We define the maximal value of any variable X as the cutoff $\Phi(X)$ of its statistical distribution. This cutoff is here obtained by approximating the tail of the corresponding cumulative distribution function (CDF) of X with a quadratic function that reaches a maximum of 1 in Φ. The least-squares fit is performed with data from quantiles 0.85–0.995.

The cutoff mass at $\tau_n < 1$ is determined for each δ and We independently [Fig. 20(b), inset]. It is remarkably independent of δ and We, and its average value is given by Eq. (21). Similarly to the droplet speed, once this cutoff mass is expressed as a function of the sheet time τ_n, any explicit dependence on We and δ disappears, which is characteristic of the droplets radially ejected during sheet expansion.

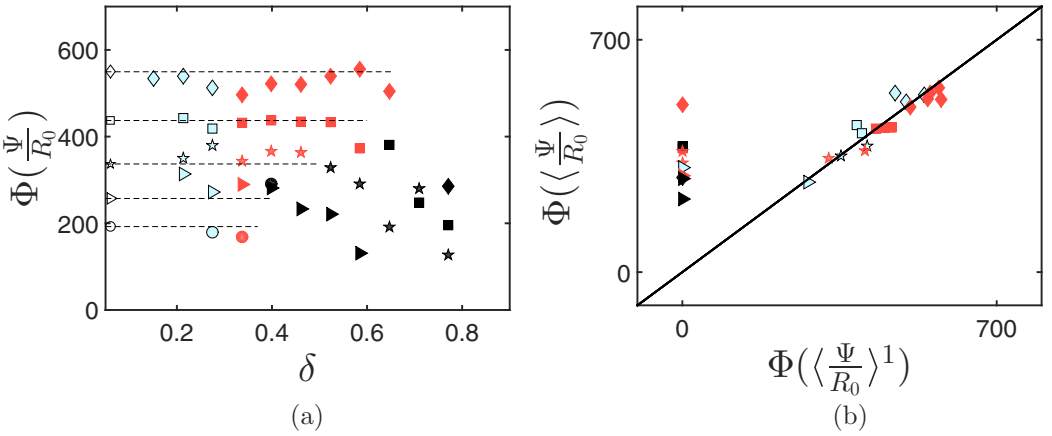

FIG. 21. (a) Maximum horizontal distance $\Phi(\Psi/R_0)$ traveled by the ejected droplets, pooled together per We and δ. Symbols correspond to different We (Table I) while colors indicate scenarios I, black; II, red (gray); and III, blue (clear). The dashed lines correspond to Eq. (22). (b) $\Phi(\Psi/R_0)$ during the whole ejection process compared to the one dictated by the droplets ejected during the sheet extension. The solid line is the bisector. Symbols correspond to the values We = 186 (◯), 367 (▷), 700 (★), 1340 (□), and 2435 (◇).

During retraction and after sheet collapse, the distribution and cutoff value of the mass are almost independent of δ and slightly decrease with increasing We. A more detailed analysis of such dependence is given in Appendix C.

D. Distance traveled by the droplets

The ballistic trajectory $\mathbf{x}(t) = x(t)\mathbf{e}_x + z(t)\mathbf{e}_z$ of each ejected droplet in a vertical plane $(\mathbf{e}_x, \mathbf{e}_z)$ can be computed from Newton's law, as a function of its mass m and ejection speed v (Appendix B). We here consider the horizontal direction of ejection $\mathbf{e}_x$ and compute $x(t)$, the distance traveled horizontally since ejection, regardless of direction θ_v. Owing to air drag, the horizontal speed decreases with time and $x(t)$ reaches an asymptotic value $\Psi = \lim_{t\to\infty} x$, the aerodynamic wall [73].

The cutoff $\Phi(\Psi)$ of the statistical distribution of Ψ is calculated by pooling all ejected droplets from different experiments at given We and δ [Fig. 21(a)]. For scenarios II and III, $\Phi(\Psi)$ is fairly independent of δ. By contrast, for scenario I, $\Phi(\Psi)$ decreases with increasing δ. The similarity of $\Phi(\langle\Psi\rangle)$ and $\Phi(\langle\Psi\rangle^1)$, illustrated in Fig. 21(b), suggests that the cutoff distance $\Phi(\Psi)$ is already reached by the droplets ejected during sheet expansion ($\tau_n < 1$), if any (i.e., for scenarios II and III). Droplets ejected afterward ($\tau_n > 1$) can travel as far, but not significantly farther. The upper bound of Ψ first increases with time, until a maximum value Ψ_M is reached slightly before $\tau_n = 1$. This maximum Ψ_M during expansion can be recovered from the maximal mass $\Phi(m/M_0)$ given by Eq. (21) and the quantile 90% of the ejection speed. Indeed, during sheet expansion, the speed distribution is approximately Gaussian with mean v_T and standard deviation $0.2v_T$ (Fig. 19), so this quantile is estimated as $Q_{90}(v_T/V_0) = [1 + 0.2\sqrt{2}\mathrm{erf}^{-1}(0.8)](v_T/V_0) = 1.26v_T/V_0$. Since both mass and speed bounds are independent of δ during sheet expansion [Figs. 19(a) and 20(b), insets], Ψ_M is also independent of δ. Droplets of scenario I are only ejected for $\tau_n > 1$, when the average speed is already low [Fig. 18(a)] while the mass is not necessarily larger (see Appendix C). As a result, the range of the droplets from scenario I is lower than that of other scenarios.

For the range of We considered in this study, Ψ_M is approximately given by

$$\frac{\Psi_M}{R_0} \simeq 23\,\mathrm{We}^{2/5}, \tag{22}$$

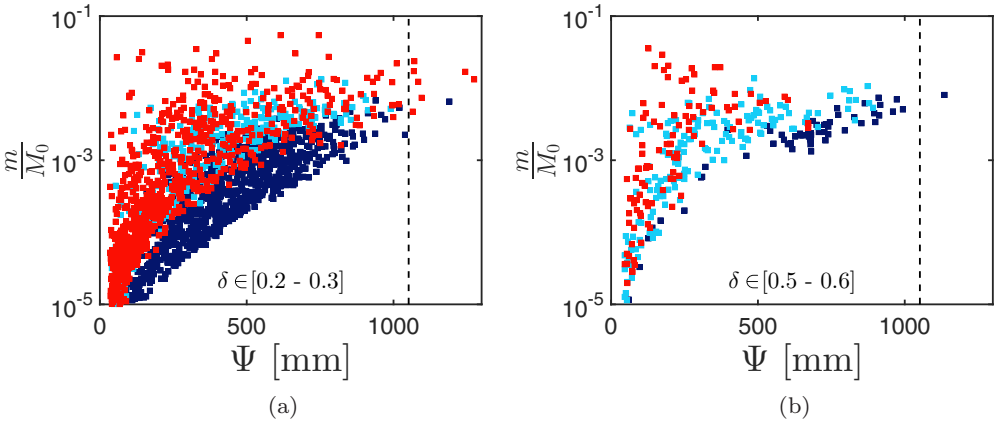

FIG. 22. Mass m of the ejected droplets, normalized by the mass of the impacting drop, as a function of their traveled distance Ψ for We = 1340 (□) and (a) $\delta \in [0.2–0.3]$ and (b) $\delta \in [0.5–0.6]$. The color indicates the ejection time: during sheet expansion ($\tau_n < 1$, dark blue), during sheet retraction ($1 < \tau_n < \tau_r$, light blue), and after sheet collapse ($\tau_n > \tau_r$, red). The vertical dotted lines represent Eq. (22).

which provides a practical first-order approximation of the distance that ejected droplets can possibly reach at a given We in the worst case scenario (scenarios II and III). This upper bound on traveled distance, originally derived from droplets ejected during sheet expansion, seems to hold for droplets ejected when the sheet retracts and collapses. This implies that the sheet's early dynamics conditions the maximum distance traveled by the droplets for scenarios II and III independently of the offset.

E. Global effects of sheet asymmetry

The preceding section showed that the maximum distance traveled by the ejected droplets is fairly insensitive to the sheet asymmetry (i.e., to the offset). However, this asymmetry still greatly influences the dispersal ability. For example, the mass of droplets ejected at a given distance Ψ (usually during sheet retraction and collapse) can be 10 times larger than the mass of droplets ejected during the sheet expansion, provided the offset is sufficiently small. This is illustrated in the (m/M_0, Ψ) diagrams of Figs. 22(a) and 22(b) for two different ranges of δ. Tangentially ejected droplets are often among these outperforming droplets, since they inherit from a mass similar to the radially ejected droplets, but with a possibly higher speed. Figure 22(a) also displays a large number of small droplets ejected during the collapse phase, which corresponds to the filament breakup mechanism.

In terms of the number of droplets, the CDF of the normalized time τ_n at which droplets are ejected, i.e., the number of droplets ejected before a given normalized time τ_n, is represented in Fig. 23(a) for the six examples of Figs. 4 and 5. The number of droplets increases with We and decreases with increasing δ. For all scenarios, the ejection rate (slope of the CDF) remains steady during sheet extension and then strongly decreases during retraction. In scenarios II and III, there is an additional outburst of droplets at the moment of collapse τ_r, which corresponds to the filament breakup mechanism. The ejection rate decreases again for larger τ_n. For scenarios II and III, the first ejections occur during the expansion of the sheet. Conversely, in the isotropic scenario I, ejections only start during the retraction of the sheet.

The average number N of ejected droplets per impact is represented in Fig. 23(b), where data from all experiments have been again pooled by We and δ. This number of droplets increases with We and decreases almost quadratically with increasing offset δ. The number of droplets vanishes in $\delta = 0.9$, which also corresponds to a vanishing liquid sheet [Eq. (8)]. These dependencies, seen in

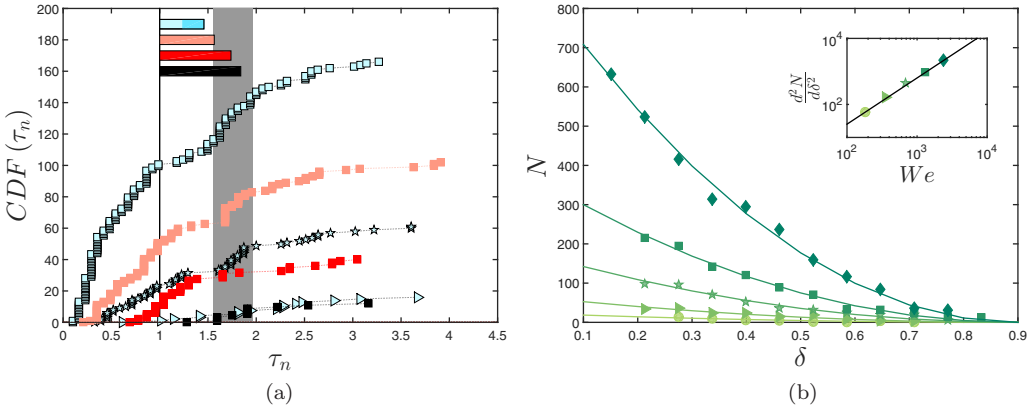

FIG. 23. (a) Non-normalized cumulative distribution function (expressed in number of ejected droplets) of the normalized time τ_n for the six examples of Figs. 4 and 5. Symbols correspond to Weber numbers We = 367 (▷), 700 (★), and 1340 (□), while colors indicate scenarios I, black; II, light and dark red (light and dark gray); and III, blue (clear). The gray area indicates the time τ_r at which the sheet has fully retracted from the edge (average across We and δ, plus or minus the standard deviation). The horizontal rectangles represent the duration of the sheet retraction. The darker blue rectangle in scenario III corresponds to the retraction of the sheet after it has pinched from the edge. (b) Average number N of droplets ejected per impact, as a function of δ, for We = 186 (◯), 367 (▷), 700 (★), 1340 (□), and 2435 (◇). Solid lines are Eq. (23). The inset shows the second derivative of N with respect to δ, as a function of We. The solid line corresponds to $d^2N/d\delta^2 = 0.04\,\mathrm{We}^{1.4}$ in Eq. (23).

Fig. 23(b), can be captured by

$$N = 0.02\,\mathrm{We}^{1.4}(0.9-\delta)^2. \tag{23}$$

The increase of the number of droplets with the decrease of δ could originate from three main causes: As δ decreases, (i) more fluid crosses the edge, (ii) the filament breakup mechanism occurs, which is responsible for a high number of small droplets, and (iii) the shedding of droplets begins earlier. The offset thus influences the number and mass of the droplets.

VI. DISCUSSION

Raindrops can impact plant leaves and subsequently fragment into droplets in many configurations. Some of these configurations are particularly efficient at ejecting droplets far away, thus shaping the dispersal of pathogens initially present on infected leaves. A common feature observed in most impact configurations is the formation and breakup of an asymmetric liquid sheet, connected to the substrate on one side and delimited by a rim entirely in the air on the other side. In this paper, we investigated the impact of a drop at speed V_0 in the vicinity of the straight edge of a flat horizontal substrate. A similar sheet forms and fragments, but its kinematics is easier to visualize and quantify since both the sheet and the ejected droplets move approximately in the plane of the substrate. Moreover, this configuration involves only two relevant dimensionless parameters: the offset from the surface edge d and the Weber number We. We varied both parameters, with the latter in a range similar to that of raindrops. From video recordings, we systematically tracked and quantified the motion of both the sheet and the ejected droplets.

The evolution of the sheet in the direction normal to the edge is approximately symmetric in time. It can be described by measuring the time from its birth, at the instant t_d at which the liquid takes off from the substrate. The duration of the sheet extension $t_{nM} - t_d$ is then approximately proportional to the capillary time t_c [Eq. (11)], with a corrective factor that mostly depends on the ratio δ between the offset d and the maximum spreading distance on the solid R_{sM}. The maximum extension l_{nM}

of the sheet normal to the edge is approximately proportional to $V_0 t_c$ [Eq. (9)], with a corrective factor to account for the history of the fluid spread on the solid. This latter is linearly decreasing with δ. Remarkably, the corresponding acceleration normal to the edge, which then scales as V_0/t_c, is constant with time and does not depend on δ. We have also shown that, contrary to intuition, the sheet can extend farther from the substrate when a drop impacts at a distance d from a flat edge than when it impacts at the center of a pole of radius d.

The evolution of the sheet along the edge is however not symmetric in time. Its extension follows the adjacent spreading on the substrate, while its retraction involves dewetting of the edge. The important scatter of the corresponding data suggests the presence of uncontrolled contact line pinning during this retraction phase. The asymmetry of the sheet shape strongly depends on δ. We identified three different scenarios, which correspond to characteristic shapes of the sheet. The boundaries between these scenarios can be rationalized by considering the competition of sheet kinematics in directions normal and tangent to the edge.

We characterized ejected droplets statistically in terms of number, mass, speed, direction, and time of ejection. The ejection statistics is time dependent and varies with δ and We. Nevertheless, most of the dependence on δ is accounted for when the rescaled ejection time τ_n (ejection time normalized by the time of maximal extension of the sheet) is used. This is especially true during sheet expansion, when droplets are mostly ejected radially starting from a time that increases with δ. Droplets ejected at the same normalized time have approximately the same speed, which decreases with this time. Their mass distribution is more scattered, but it is bounded by a maximal ejectable mass that is an increasing function of τ_n only.

When the sheet retracts and collapses, both droplet speed and mass distributions spread considerably (at least for the two most asymmetrical sheet scenarios) and depend on δ. This is partly due to the additional ejection of tangentially ejected droplets, i.e., droplets ejected in a direction parallel to the sheet and normal to its retraction. In the most asymmetrical cases (small δ), the final collapse of the sheet near the edge triggers out-of-plane ejection of a large number of tiny droplets.

We estimated the maximum horizontal distance that each ejected droplet would travel ballistically, as a function of its mass and ejection speed. The upper bound of this distance is independent of δ for the two most asymmetric sheet scenarios. It can be predicted by considering the speed and maximum mass of droplets ejected during the sheet expansion only. Droplets ejected during the retraction and collapse of the sheet can go as far, but not significantly farther. However, for the same traveled distance, their mass can be larger by a factor of 10. The decrease in offset allows these larger droplets to increase their distance traveled while staying bounded by the distance predicted by the sheet early dynamics.

These results can be discussed in the context of rain-induced dispersal of foliar pathogens. Each droplet ejected from an infected leaf is susceptible to carry some pathogenic content. The number, mass, and ejection speed of these droplets are key inputs for epidemiological models aiming to capture the physics of transfers [74]. The likelihood of infection is a combination of these factors. Our experiments at We $\in [180, 2500]$ covered most of the range of Weber number experienced by raindrops (We $\in [28, 5800]$). We may therefore expect that our conclusions on the impact near a straight edge are still valid, at least qualitatively, for more complex impact scenarios encountered by raindrops on leaves. In particular, the number, the speed of the ejected droplets, and their maximal traveled distance all increase with increasing We, while the maximal droplet mass decreases. The asymmetry of the sheet, omnipresent in complex natural impacts, does not appear to increase the maximum distance traveled by the droplets, but instead, increases their number and maximal mass that reaches a given distance. The asymmetry of the sheet, measured by δ here, should consequently increase the likelihood that a droplet containing a critical amount of pathogens lands on a leaf at a given distance, potentially increasing the overall disease dispersal in a field.

The risk of epidemics is a major factor to take into account in the optimization of crops [75]. Current mitigation techniques of foliar diseases, such as the intensive use of chemicals or genetically modified organisms, can be complemented by polyculture [13,75,76] or integrated culture [77]. Our work has shown how both impact speed and distance from an edge shape the statistics of ejected

droplets upon raindrop impact. Our results can help the development of agricultural epidemiological models rooted in important mechanistic and physical processes.

ACKNOWLEDGMENTS

This work was supported by the FRIA/FNRS and the USDA-NIFA Specialty Crop Research Initiative Grant Award No. MDW-2016-04938, MIT REED and Edgerton Funds. S.L. is grateful for support from the Rotary Foundation. The authors also thank L. Tadrist and Y. Wang for fruitful discussions.

APPENDIX A: DROPLET TRACKING AND MASS CALCULATION

On each frame, all the objects detached from the main body of the sheet were considered as ejected droplets. Their area, perimeter, and position with respect to the impact point were recorded. Their trajectory was then reconstructed. During this process, only objects that could be consistently tracked over at least five frames were considered. This condition removed fluid particles that either quickly merged with others or that quickly fragmented. The ejection time of the droplets is defined as the time at which they were first detected. The ejection velocity $\mathbf{v}$ is calculated from the first frames after ejection. Merging and fragmentation of droplets are common, especially during sheet retraction in the most asymmetrical scenarios (II and III). We chose to only consider as droplets the objects that either left the field of view before the end of the recording or were still present in its last frame. By doing so, we reduced the likelihood of counting multiple times the same fluid particle. However, we also arbitrarily selected large merged droplets instead of keeping the smaller droplets that were initially ejected. Furthermore, sometimes the residues of the collapsed sheet did not fully fragment by the time they left the field of view.

Estimating the mass m of the ejected droplets is challenging. Indeed, they are highly deformed when they pinch off from the liquid sheet and they need some additional time to relax to a quasispherical equilibrium shape resulting from a balance of aerodynamic drag and surface tension [57]. This relaxation time is of the order of r^2/ν, where r is such that $m/\rho = 4\pi r^3/3$. Moreover, droplet collisions are common, especially when the high asymmetry of the sheet leads to antagonist motions of the rim. It is therefore likely that the tracked droplets leave the field of view before they become spherical.

We here estimate the droplet volume $\Omega = m/\rho$ based on a combination of the perimeter P and the area A seen and measured on each image. A droplet pinching off from a fluid ligament is initially elongated, so at first order it can be approximated by a pill shape, i.e., a cylinder of length L and radius R surrounded by two spherical caps of radius R. When $L \gg R$, Ω, A, and P are proportional to R^2L, RL, and L, respectively, so the ratio $\Omega P/A^2$ should be constant. In general (for any L and R),

$$\frac{\Omega P}{A^2} = \frac{2\pi x^2 + \left(2\pi^2 + \frac{8\pi}{3}\right)x + \frac{8\pi^2}{3}}{4x^2 + 4\pi x + \pi^2}, \tag{A1}$$

where $x = L/R$. The ratio $\Omega P/A^2$ indeed tends to a constant value of $\pi/2$ for an elongated pill ($x \gg 1$). In the other limit of a quasispherical pill ($x \ll 1$), $\Omega P/A^2 \simeq 8/3$, which is slightly larger. More complicated elongated shapes, such as when the sheet collapses after separation from the edge (scenario III), could be seen as a sum of elongated droplets, and it is likely that their ratio $\Omega P/A^2$ remains in the range $[\pi/2, 8/3]$.

In order to estimate the droplet volume, we first calculate an approximation of x. Since $P = 2R(\pi + x)$ and $A = R^2(\pi + 2x)$, x satisfies the second-order equation

$$x^2 + 2\left(\pi - \frac{P^2}{4A}\right)x + \pi\left(\pi - \frac{P^2}{4A}\right) = 0. \tag{A2}$$

This equation admits a single positive solution x when $P^2 \geqslant 4\pi A$ (the equality yields a spherical droplet). The volume is then calculated from Eq. (A1).

In conventional image processing functions (e.g., in MATLAB), A is calculated as the sum of the selected pixels, while P is calculated by joining the centers of the edge pixels. Consequently, A is overestimated compared to P, which may erroneously result in $P^2 < 4\pi A$. This artifact may be corrected by removing the excess of area, i.e., by replacing A by $A - \epsilon P/2$, where ϵ is the pixel size. This correction is sufficient to ensure $P^2 \geqslant 4\pi A$ for all droplets.

APPENDIX B: DISTANCE TRAVELED TO THE AERODYNAMIC WALL

The ballistic trajectory $\mathbf{x}(t) = x(t)\mathbf{e}_x + z(t)\mathbf{e}_z$ of each ejected droplet can be computed from Newton's law, as a function of its mass m and ejection speed v,

$$\begin{aligned} m\frac{d^2\mathbf{x}}{dt^2} &= -mg\mathbf{e}_z - 6\pi\mu_a r\frac{d\mathbf{x}}{dt}\left[1 + \frac{c}{100}\mathrm{Re}^{2/3}\right] \quad \text{for } \mathrm{Re} = \frac{2r\rho_a}{\mu_a}\left|\frac{d\mathbf{x}}{dt}\right| < 1000, \\ m\frac{d^2\mathbf{x}}{dt^2} &= -mg\mathbf{e}_z - \frac{3(1+c)}{125}\frac{\pi}{2}\rho_a r^2\frac{d\mathbf{x}}{dt}\left|\frac{d\mathbf{x}}{dt}\right| \quad \text{for } \mathrm{Re} > 1000, \end{aligned} \tag{B1}$$

where Re is the Reynolds number, $r = (3m)^{1/3}/(4\pi\rho)^{1/3}$ is the droplet radius, c is a fitting parameter, and ρ_a and μ_a are the density and dynamic viscosity of the air, respectively. We here consider $\mathbf{e}_x$ as the horizontal direction of ejection, and $x(t)$ is the distance traveled horizontally since ejection, no matter in which direction θ_v. In Eq. (B1), the air drag is calculated with an approximation valid for spherical objects in a large range of Reynolds number (cf. similar models in Ref. [78]). A fit on experimental data from [79] yields $c \simeq 16$.

Owing to air drag, the horizontal speed decreases with time and $x(t)$ reaches an asymptotic value $\Psi = \lim_{t\to\infty} x$ called the aerodynamic wall [73]. Equation (B1) is nondimensionalized with characteristic timescale T and length scale L defined in the limit of small Reynolds number, $T = 2\rho r^2/(9\mu_a)$, $L = gT^2$, $\mathbf{y} = \mathbf{x}/L$, and $\tau = t/T$ from which we obtain

$$\begin{aligned} \frac{d^2\mathbf{y}}{d\tau^2} &= -\mathbf{e}_z - \left[1 + \frac{c}{100}\beta^{2/3}\left|\frac{d\mathbf{y}}{dt}\right|^{2/3}\right]\frac{d\mathbf{y}}{d\tau} \quad \text{if } \beta\left|\frac{d\mathbf{y}}{dt}\right| < 1000, \\ \frac{d^2\mathbf{y}}{d\tau^2} &= -\mathbf{e}_z - \frac{1+c}{1000}\beta\left|\frac{d\mathbf{y}}{dt}\right|\frac{d\mathbf{y}}{d\tau} \quad \text{if } \beta\left|\frac{d\mathbf{y}}{dt}\right| > 1000, \end{aligned} \tag{B2}$$

where the dimensionless parameter β is defined as $\beta = mg\rho_a/(3\pi\mu_a^2) = 4\rho_a\rho g r^3/(9\mu_a^2)$. This differential equation can be integrated, with an initial horizontal dimensionless speed $d\mathbf{y}/d\tau|_{\tau=0} \cdot \mathbf{e}_x = u = 9\mu_a/(2\rho g r^2 v)$.

1. Exact solution at low Reynolds number

There is an exact solution to Eq. (B2) at low Reynolds number, i.e., for droplets that are sufficiently small so $\beta \ll 1$. Equation (B2) then simplifies into

$$\frac{d^2\mathbf{y}}{d\tau^2} + \frac{d\mathbf{y}}{d\tau} = -\mathbf{e}_z. \tag{B3}$$

Time integration yields $\mathbf{y} = (1 - e^{-\tau})(u\mathbf{e}_x + \mathbf{e}_z) - \tau\mathbf{e}_z$. The maximum horizontal distance traveled is then $y_\infty = \lim_{\tau\to\infty} \mathbf{y}\cdot\mathbf{e}_x = u$ or, in dimensional form, $\Psi_0 = \Psi(\beta \ll 1) = y_\infty L = 2\rho r^2 v/(9\mu_a)$. The condition $\mathrm{Re} < 1$ yields

$$\frac{2r\rho_a L}{\mu_a T} < 1 \Rightarrow \beta < 1. \tag{B4}$$

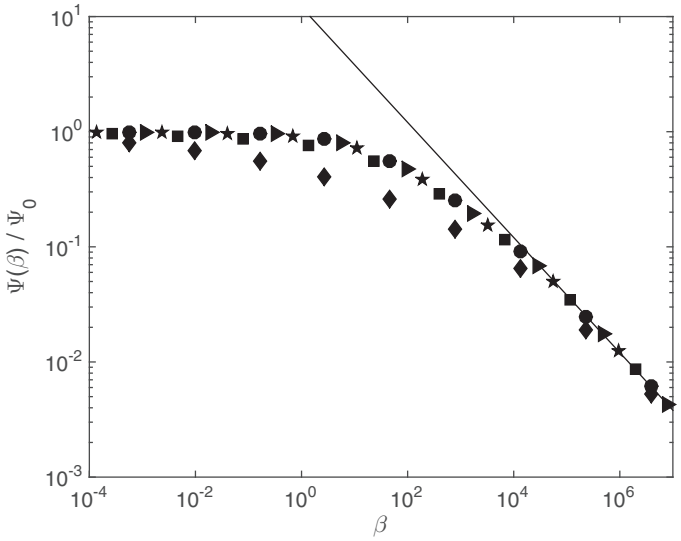

FIG. 24. Maximum traveled horizontal distance Ψ, as a function of the dimensionless droplet size β. Each symbol corresponds to a different ejection speed v: ◯, $v = 10^{-3}$ m/s; ▷, $v = 10^{-2}$ m/s; ★, $v = 10^{-1}$ m/s; □, $v = 1$ m/s; and ◇, $v = 10$ m/s. The solid line corresponds to $\Psi(\beta)/\Psi(0) \simeq 12\beta^{-1/2}$.

2. Numerical solution for any Reynolds number

The droplets ejected during the sheet fragmentation are in the range $m/M_0 \in [3 \times 10^{-6}, 3 \times 10^{-2}]$ [Fig. 20(a)], which corresponds to $r \in [0.035, 0.75]$ mm and $\beta \in [0.67, 6700]$. The ejection speed can reach 10 m/s, so the Reynolds number at ejection can be as high as 1000. Therefore, we need to solve Eq. (B2) numerically.

The solution is represented for dimensionless size $\beta \in [10^{-4}, 10^{7}]$ and ejection speed $v \in [10^{-3}, 10]$ m/s, in Fig. 24. Once normalized by Ψ_0, the aerodynamic wall Ψ does not depend on ejection speed v anymore, except for very large speed (here $v = 10$ m/s), where Ψ/Ψ_0 can be half as large as at moderate speed. So in a first approximation

$$\frac{\Psi}{\Psi_0} = F(\beta), \tag{B5}$$

where $F(\beta) \to 1$ for $\beta \to 0$ and $F(\beta) \to 12/\sqrt{\beta}$ when $\beta \to \infty$.

The function $F(\beta)$ satisfies $F(0) = 1$ (low Reynolds limit) and scales as $F \sim \beta^{-1/2}$ for $\beta \gg 1$ (high Reynolds limit). Since β is only dependent on droplet size r and not on speed v, the aerodynamic wall at a distance Ψ is always approximately proportional to the ejection speed v.

APPENDIX C: DROPLET MASSES AFTER MAXIMUM EXTENSION

During retraction, the mass distribution is almost independent of δ, and it is slightly shifted to lower mass with increasing We. By contrast, the distribution after collapse does depend on both δ and We. The cutoff Φ of the mass distribution of ejected droplets is again calculated separately for each We and δ, first during sheet retraction [Fig. 25(a)] and second after sheet collapse [Fig. 25(b)]. During retraction, the variation of $\Phi(\langle m/M_0\rangle^2)$ with δ is very small. Consequently, data from different δ can be pooled, which reveals a power-law dependence on We [Fig. 25(a), inset] given by

$$\Phi\left(\overline{\left\langle \frac{m}{M_0} \right\rangle}^2\right) \simeq 2.9\,\mathrm{We}^{-3/4}. \tag{C1}$$

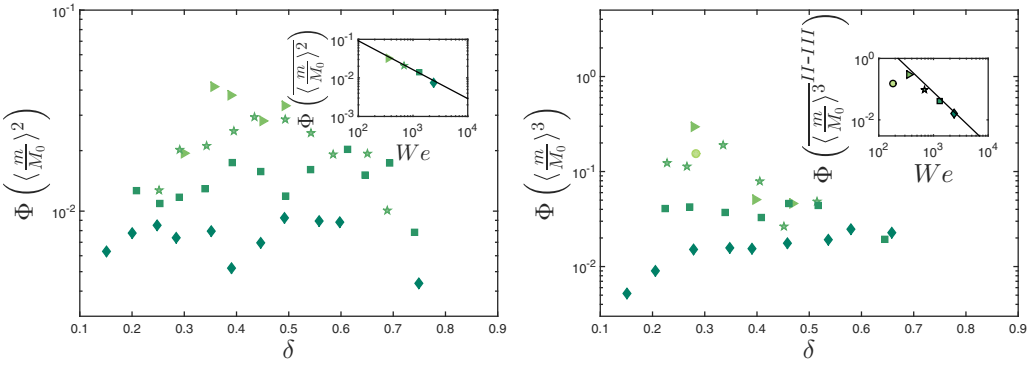

(a) (b)

FIG. 25. Cutoff Φ of the mass distribution of ejected droplets, pooled per We and δ, (a) during the retraction of the sheet and (b) after collapse of the sheet, for the values We = 186 (◯), 367 (▷), 700 (★), 1340 (□), and 2435 (◇). The insets show the dependence on We of the cutoff Φ (a) after pooling all δ [the solid line is Eq. (C1)] and (b) after pooling scenarios II and III [the solid line is Eq. (C2)].

After the collapse of the sheet, $\Phi(\langle m/M_0 \rangle^3)$ is almost independent of δ at high We, but it sharply decreases with increasing δ at lower We. The pooling of scenarios II and III reveals a decrease of the average cutoff with increasing We given by

$$\Phi\left(\overline{\left\langle \frac{m}{M_0} \right\rangle^3}^{\text{II–III}}\right) \simeq 10^4 \text{We}^{-1.7}. \tag{C2}$$

The comparison of Eqs. (C1) and (C2) reveals that, for We $\lesssim$ 4000, the mass cutoff is larger after collapse than during retraction of the sheet. This fact could be the consequence of (i) the likely merging of ejected droplets after collapse and (ii) the presence of a very large liquid filament detached from the edge (e.g., in scenario III) that does not instantly destabilize into smaller droplets.

[1] E.-C. Oerke, Crop losses to pests, J. Agric. Sci. **144**, 31 (2006).

[2] I. B. Pangga, J. Hanan, and S. Chakraborty, Pathogen dynamics in a crop canopy and their evolution under changing climate, Plant Pathol. **60**, 70 (2011).

[3] H. Fones and S. Gurr, The impact of Septoria tritici blotch disease on wheat: An EU perspective, Fungal Genet. Biol. **79**, 3 (2015).

[4] R. D. Magarey, T. B. Sutton, and C. L. Thayer, A simple generic infection model for foliar fungal plant pathogens, Phytopathology **95**, 92 (2005).

[5] A. Dalla Marta, R. D. Magarey, and S. Orlandini, Modelling leaf wetness duration and downy mildew simulation on grapevine in italy, Agric. For. Meteorol. **132**, 84 (2005).

[6] A. Calonnec, J.-B. Burie, M. Langlais, S. Guyader, S. Saint-Jean, I. Sache, and B. Tivoli, Impacts of plant growth and architecture on pathogen processes and their consequences for epidemic behaviour, Eur. J. Plant Pathol. **135**, 479 (2013).

[7] G. Garin, C. Fournier, B. Andrieu, V. Houlès, C. Robert, and C. Pradal, A modeling framework to simulate foliar fungal epidemics using functional-structural plant models, Ann. Bot. **114**, 795 (2014).

[8] B. D. L. Fitt, H. A. McCartney, and P. J. Walklate, The role of rain in dispersal of pathogen inoculum, Annu. Rev. Phytopathol. **27**, 241 (1989).

[9] P. A. Paul, S. M. El-Allaf, P. E. Lipps, and L. V. Madden, Rain splash dispersal of *Gibberella zeae* within wheat canopies in Ohio, Phytopathology **94**, 1342 (2004).
[10] G. N. Agrios, *Plant Pathology* (Elsevier, London, 2005).
[11] P. J. Walklate, H. A. McCartney, and B. D. L. Fitt, Vertical dispersal of plant pathogens by splashing. Part II: Experimental study of the relationship between raindrop size and the maximum splash height, Plant Pathol. **38**, 64 (1989).
[12] X. Yang, L. V. Madden, L. L. Wilson, and M. A. Ellis, Effects of surface topography and rain intensity on splash dispersal of Colletotrichum acutatum, Phytopathology **80**, 1115 (1990).
[13] C. Gigot, S. Saint-Jean, L. Huber, C. Maumené, M. Leconte, B. Kerhornou, and C. de Vallavieille-Pope, Protective effects of a wheat cultivar mixture against splash-dispersed septoria tritici blotch epidemics, Plant Pathol. **62**, 1011 (2013).
[14] K. M. Reynolds, M. A. Bulger, L. V. Madden, and M. A. Ellis, New methods using simulated rain to study the splash dispersal of plant pathogens, Phytopathology **77**, 921 (1987).
[15] X. Yang, L. V. Madden, D. L. Reichard, R. D. Fox, and M. A. Ellis, Motion analysis of drop impaction on a strawberry surface, Agric. For. Meteorol. **56**, 67 (1991).
[16] I. Sache, Short-distance dispersal of wheat rust spores by wind and rain, Agronomie **20**, 757 (2000).
[17] S. Pietravalle, F. Van Den Bosch, S. J. Welham, S. R. Parker, and D. J. Lovell, Modelling of rain splash trajectories and prediction of rain splash height, Agric. For. Meteorol. **109**, 171 (2001).
[18] T. Gilet and L. Bourouiba, Rain-induced ejection of pathogens from leaves: Revisiting the hypothesis of splash-on-film using high-speed visualization, Integr. Comp. Biol. **54**, 974 (2014).
[19] T. Gilet and L. Bourouiba, Fluid fragmentation shapes rain-induced foliar disease transmission, J. R. Soc. Interface **12**, 20141092 (2015).
[20] A. L. Yarin, Drop impact dynamics: Splashing, spreading, receding, bouncing.Annu. Rev. Fluid Mech. **38**, 159 (2006).
[21] M. Marengo, C. Antonini, I. V. Roisman, and C. Tropea, Drop collisions with simple and complex surfaces, Curr. Opin. Colloid Interface Sci. **16**, 292 (2011).
[22] C. Josserand and S. T. Thoroddsen, Drop impact on a solid surface, Annu. Rev. Fluid Mech. **48**, 365 (2016).
[23] A.-B. Wang and C.-C. Chen, Splashing impact of a single drop onto very thin liquid films, Phys. Fluids **12**, 2155 (2000).
[24] C. Josserand and S. Zaleski, Droplet splashing on a thin liquid film, Phys. Fluids **15**, 1650 (2003).
[25] R. Rioboo, C. Bauthier, J. Conti, M. Voué, and J. De Coninck, Experimental investigation of splash and crown formation during single drop impact on wetted surfaces, Exp. Fluids **35**, 648 (2003).
[26] M. Rein, Phenomena of liquid drop impact on solid and liquid surfaces, Fluid Dyn. Res. **12**, 61 (1993).
[27] B. Ray, G. Biswas, and A. Sharma, Regimes during liquid drop impact on a liquid pool, J. Fluid Mech. **768**, 492 (2015).
[28] R. Rioboo, C. Tropea, and M. Marengo, Outcomes from a drop impact on solid surfaces, Atomiz. Sprays **11**, 155 (2001).
[29] M. Reyssat, A. Pépin, F. Marty, Y. Chen, and D. Quéré, Bouncing transitions on microtextured materials, Europhys. Lett. **74**, 306 (2006).
[30] C. Antonini, A. Amirfazli, and M. Marengo, Drop impact and wettability: From hydrophilic to superhydrophobic surfaces, Phys. Fluids **24**, 102104 (2012).
[31] P. K. Unnikrishnan, V. Vaikuntanathan, and D. Sivakumar, Impact dynamics of high weber number drops on chemically modified metallic surfaces, Colloids Surf. A **459**, 109 (2014).
[32] D. Khojasteh, M. Kazerooni, S. Salarian, and R. Kamali, Droplet impact on superhydrophobic surfaces: A review of recent developments, J. Ind. Eng. Chem. **42**, 1 (2016).
[33] Z. Levin and P. V. Hobbs, Splashing of water drops on solid and wetted surfaces, hydrodynamics and charge separation, Philos. Trans. R. Soc. London Ser. A **269**, 555 (1971).
[34] S. Mandre, M. Mani, and M. P. Brenner, Precursors to Splashing of Liquid Droplets on a Solid Surface, Phys. Rev. Lett. **102**, 134502 (2009).
[35] J. Palacios, J. Hernández, P. Gómez, C. Zanzi, and J. López, Experimental study of splashing patterns and the splashing/deposition threshold in drop impacts onto dry smooth solid surfaces, Exp. Therm. Fluid Sci. **44**, 571 (2013).

[36] G. Riboux and J. M. Gordillo, Experiments of Drops Impacting a Smooth Solid Surface: A Model of the Critical Impact Speed for Drop Splashing, Phys. Rev. Lett. **113**, 024507 (2014).
[37] G. Riboux and J. M. Gordillo, The diameters and velocities of the droplets ejected after splashing, J. Fluid Mech. **772**, 630 (2015).
[38] A. Rozhkov, B. Prunet-Foch, and M. Vignes-Adler, Impact of water drops on small targets, Phys. Fluids **14**, 3485 (2002).
[39] E. Villermaux and B. Bossa, Drop fragmentation on impact, J. Fluid Mech. **668**, 412 (2011).
[40] C. Vernay, L. Ramos, and C. Ligoure, Free radially expanding liquid sheet in air: Time-and space-resolved measurement of the thickness field, J. Fluid Mech. **764**, 428 (2015).
[41] S. Arora, C. Ligoure, and L. Ramos, Interplay between viscosity and elasticity in freely expanding liquid sheets, Phys. Rev. Fluids **1**, 083302 (2016).
[42] Y. Wang and L. Bourouiba, Drop impact on small surfaces: Thickness and velocity profiles of the expanding sheet in the air, J. Fluid Mech. **814**, 510 (2017).
[43] I. V. Roisman, Dynamics of inertia dominated binary drop collisions, Phys. Fluids **16**, 3438 (2004).
[44] I. V. Roisman, C. Planchette, E. Lorenceau, and G. Brenn, Binary collisions of drops of immiscible liquids, J. Fluid Mech. **690**, 512 (2012).
[45] M. Reyssat, F. Pardo, and D. Quéré, Drops onto gradients of texture, Europhys. Lett. **87**, 36003 (2009).
[46] B. A. Malouin, Jr., N. A. Koratkar, A. H. Hirsa, and Z. Wang, Directed rebounding of droplets by microscale surface roughness gradients, Appl. Phys. Lett. **96**, 234103 (2010).
[47] V. Vaikuntanathan, R. Kannan, and D. Sivakumar, Impact of water drops onto the junction of a hydrophobic texture and a hydrophilic smooth surface, Colloids Surf. A **369**, 65 (2010).
[48] J. C. Bird, R. Dhiman, H.-M. Kwon, and K. K. Varanasi, Reducing the contact time of a bouncing drop, Nature (London) **503**, 385 (2013).
[49] D. H. Kwon, H. K. Huh, and S. J. Lee, Wettability and impact dynamics of water droplets on rice (*Oryza sativa* L.) leaves, Exp. Fluids **55**, 1691 (2014).
[50] R. Zhang, P. Hao, and F. He, Drop impact on oblique superhydrophobic surfaces with two-tier roughness, Langmuir **33**, 3556 (2017).
[51] J. C. Bird, S. H. Tsai, and H. A. Stone, Inclined to splash: Triggering and inhibiting a splash with tangential velocity, New J. Phys. **11**, 063017 (2009).
[52] Y. H. Yeong, J. Burton, E. Loth, and I. S. Bayer, Drop impact and rebound dynamics on an inclined superhydrophobic surface, Langmuir **30**, 12027 (2014).
[53] H. Fujimoto, S. Yoshimoto, K. Takahashi, T. Hama, and H. Takuda, Deformation behavior of two droplets successively impinging obliquely on hot solid surface, Exp. Therm. Fluid Sci. **81**, 136 (2017).
[54] G. Juarez, T. Gastopoulos, Y. Zhang, M. L. Siegel, and P. E. Arratia, Splash control of drop impacts with geometric targets, Phys. Rev. E **85**, 026319 (2012).
[55] Y. Liu, M. Andrew, J. Li, J. M. Yeomans, and Z. Wang, Symmetry breaking in drop bouncing on curved surfaces, Nat. Commun. **6**, 10034 (2015).
[56] N. Bremond and E. Villermaux, Atomization by jet impact, J. Fluid Mech. **549**, 273 (2006).
[57] É. Reyssat, F. Chevy, A.-L. Biance, L. Petitjean, and D. Quéré, Shape and instability of free-falling liquid globules, Europhys. Lett. **80**, 34005 (2007).
[58] E. Villermaux and B. Bossa, Single-drop fragmentation determines size distribution of raindrops, Nat. Phys. **5**, 697 (2009).
[59] I. V. Roisman, C. M. Weickgenannt, A. N. Lembach, and C. Tropea, *Proceedings of the 23rd Annual Conference on Liquid Atomization and Spray Systems, Brno, 2010* (Tribun, Brno, 2010).
[60] C. Duez, C. Ybert, C. Clanet, and L. Bocquet, Wetting Controls Separation of Inertial Flows from Solid Surfaces, Phys. Rev. Lett. **104**, 084503 (2010).
[61] See Supplemental Material at http://link.aps.org/supplemental/10.1103/PhysRevFluids.3.083601 for videos.
[62] R. Rioboo, M. Marengo, and C. Tropea, Time evolution of liquid drop impact onto solid, dry surfaces, Exp. Fluids **33**, 112 (2002).
[63] A. L. Yarin and D. A. Weiss, Impact of drops on solid surfaces: Self-similar capillary waves, and splashing as a new type of kinematic discontinuity, J. Fluid Mech. **283**, 141 (1995).

[64] I. V. Roisman, R. Rioboo, and C. Tropea, Normal impact of a liquid drop on a dry surface: Model for spreading and receding, Proc. R. Soc. A **458**, 1411 (2002).
[65] J. Eggers, M. A. Fontelos, C. Josserand, and S. Zaleski, Drop dynamics after impact on a solid wall: Theory and simulations, Phys. Fluids **22**, 062101 (2010).
[66] H. Lastakowski, F. Boyer, A.-L. Biance, C. Pirat, and C. Ybert, Bridging local to global dynamics of drop impact onto solid substrates, J. Fluid Mech. **747**, 103 (2014).
[67] N. Laan, K. G. de Bruin, D. Bartolo, C. Josserand, and D. Bonn, Maximum Diameter of Impacting Liquid Droplets, Phys. Rev. Appl. **2**, 044018 (2014).
[68] G. Lagubeau, M. A. Fontelos, C. Josserand, A. Maurel, V. Pagneux, and P. Petitjeans, Spreading dynamics of drop impacts, J. Fluid Mech. **713**, 50 (2012).
[69] A.-L. Biance, F. Chevy, C. Clanet, G. Lagubeau, and D. Quéré, On the elasticity of an inertial liquid shock, J. Fluid Mech. **554**, 47 (2006).
[70] M. Andrew, J. M. Yeomans, and D. O. Pushkin, A solvable model of axisymmetric and non-axisymmetric droplet bouncing, Soft Matter **13**, 985 (2017).
[71] F. Blanchette and T. P. Bigioni, Partial coalescence of drops at liquid interfaces, Nat. Phys. **2**, 254 (2006).
[72] T. Gilet, K. Mulleners, J. P. Lecomte, N. Vandewalle, and S. Dorbolo, Critical parameters for the partial coalescence of a droplet, Phys. Rev. E **75**, 036303 (2007).
[73] C. Cohen, B. Darbois-Texier, G. Dupeux, E. Brunel, D. Quéré, and C. Clanet, The aerodynamic wall, Proc. R. Soc. A **470**, 20130497 (2013).
[74] S. Saint-Jean, M. Chelle, and L. Huber, Modelling water transfer by rain-splash in a 3D canopy using Monte Carlo integration, Agric. For. Meteorol. **121**, 183 (2004).
[75] T. Vidal, A.-L. Boixel, B. Durand, C. de Vallavieille-Pope, L. Huber, and S. Saint-Jean, Reduction of fungal disease spread in cultivar mixtures: Impact of canopy architecture on rain-splash dispersal and on crop microclimate, Agric. For. Meteorol. **246**, 154 (2017).
[76] M. S. Wolfe, Crop strength through diversity, Nature (London) **406**, 681 (2000).
[77] A. C. Newton, C. Gravouil, and J. M. Fountaine, Managing the ecology of foliar pathogens: Ecological tolerance in crops, Ann. Appl. Biol. **157**, 343 (2010).
[78] R. Clift, J. R. Grace, and M. Weber, *Bubbles, Drops, and Particles* (Academic, London, 1978).
[79] Z. Duan, B. He, and Y. Duan, Sphere drag and heat transfer, Sci. Rep. **5**, 12304 (2015).